



Year: 2020

CD90+CD146+ identifies a pulmonary mesenchymal cell subtype with both immune modulatory and perivascular-like function in postnatal human lung

Wang, Limei ; Dorn, Patrick ; Zeinali, Soheila ; Froment, Laurène ; Berezowska, Sabina ; Kocher, Gregor J ; Alves, Marco P ; Brügger, Melanie ; Esteves, Blandina I O ; Blank, Fabian ; Wotzkow, Carlos ; Steiner, Selina ; Amacker, Mario ; Peng, Ren-Wang ; Marti, Thomas Michael ; Guenat, Olivier T ; Bode, Peter Karl ; Moehrlen, Ueli ; Schmid, Ralph Alexander ; Hall, Sean Ralph Robert

Abstract: Background: Our understanding of mesenchymal cell subsets and their function in human lung affected by aging and in certain disease settings remain poorly described. Methods: We use a combination of polychromatic flow cytometry, prospective cell-sorting strategies, confocal imaging, and modeling of microvessel formation using advanced microfluidic chip technology to characterize mesenchymal cell subtypes in human postnatal and adult lung. Tissue was obtained from patients undergoing elective surgery for congenital pulmonary airway malformations (CPAM) and other airway abnormalities including chronic obstructive pulmonary disease (COPD). Results: Using polychromatic flow cytometry, there was a 5-fold higher fraction of EpCAM-CD45-CD31-CD14- (mesenchymal) compared with EpCAM+CD45-CD31-CD14- cells (epithelial) in unaffected postnatal human lung. The mesenchymal fraction was composed primarily of single CD90+ and CD90+CD73+ cells both enriched in niche factors CXCL12 and PDGFR. Immunofluorescence confirmed CD90+ cells in close proximity to EpCAM+ cells some co-staining for pro-SPC in the alveolar region suggestive of an alveolar unit. Contained within the CD90+ population, a subset co-expressed the pericyte marker CD146 with immunomodulatory properties able to internalize influenza viroosomes, as well as live influenza virus. Postnatal CD90+CD146+ mesenchymal cells supported microvessel formation, whereas CD90+CD146+ mesenchymal cells from COPD patients failed to do so. In congenital lung lesions, cystic airspaces and dysplastic alveolar regions were marked with an expanded underlying thick interstitium of CD90+ and CD90+PDGFR+ cells. Conclusion: These data provide important new information regarding the immunophenotypic identity of key mesenchymal lineages and track their change in diverse setting of congenital lung lesions and other airway abnormalities including COPD.

DOI: <https://doi.org/10.1152/ajplung.00146.2019>

Posted at the Zurich Open Repository and Archive, University of Zurich

ZORA URL: <https://doi.org/10.5167/uzh-186505>

Journal Article

Accepted Version

Originally published at:

Wang, Limei; Dorn, Patrick; Zeinali, Soheila; Froment, Laurène; Berezowska, Sabina; Kocher, Gregor J; Alves, Marco P; Brügger, Melanie; Esteves, Blandina I O; Blank, Fabian; Wotzkow, Carlos; Steiner, Selina; Amacker, Mario; Peng, Ren-Wang; Marti, Thomas Michael; Guenat, Olivier T; Bode, Peter Karl; Moehrlen, Ueli; Schmid, Ralph Alexander; Hall, Sean Ralph Robert (2020). CD90+CD146+ identifies

a pulmonary mesenchymal cell subtype with both immune modulatory and perivascular-like function in postnatal human lung. *American Journal of Physiology. Lung Cellular and Molecular Physiology*, 318(4):L813-L830.
DOI: <https://doi.org/10.1152/ajplung.00146.2019>

CD90⁺CD146⁺ identifies a pulmonary mesenchymal cell subtype with both immune modulatory and perivascular-like function in postnatal human lung

Limei Wang^{1,2*}, Patrick Dorn^{1*}, Soheila Zeinali³, Laurène Froment^{1,2}, Sabina Berezowska⁴, Gregor J. Kocher¹, Marco P. Alves^{5,6}, Melanie Brügger^{5,6}, Blandina I.O. Esteves^{5,6}, Fabian Blank^{2,7,8}, Carlos Wotzkow⁷, Selina Steiner⁷, Mario Amacker⁹, Ren-Wang Peng^{1,2}, Thomas M. Marti^{1,2}, Olivier T. Guenat^{1,3,8}, Peter K. Bode¹⁰, Ueli Moehrlen¹¹, Ralph A. Schmid^{1,2*} and Sean R.R. Hall^{1,2}

* LW and PD contributed equally to this work

¹Department of General Thoracic Surgery, Inselspital, Bern University Hospital, University of Bern, Switzerland

²Department of BioMedical Research, University of Bern, Switzerland

³Organs-on-chip Technologies Laboratory, ARTORG Center, University of Bern, Switzerland

⁴Institute of Pathology, University of Bern, Bern, Switzerland

⁵Department of Infectious Diseases and Pathobiology, University of Bern, Switzerland

⁶Institute of Virology and Immunology, University of Bern, Switzerland

⁷DBMR Live Imaging Core Facility, University of Bern, Switzerland

⁸Department of Pulmonary Medicine, Inselspital, Bern University Hospital, University of Bern, Switzerland

⁹Mymetics SA, Epalinges, Switzerland

¹⁰Department of Pathology and Molecular Pathology, University Hospital Zurich, Switzerland

¹¹Department of Pediatric Surgery, University Children's Hospital Zurich, Zurich, Switzerland

Address correspondence to Sean R.R. Hall, PhD ¹Department of General Thoracic Surgery, Inselspital, Bern University Hospital and ²Department of BioMedical Research, University of Bern, Murtenstrasse 50, 3008 Bern, Switzerland

Tel. +41 031 632 2300

Fax. +41 031 632 2327

Email: Sean.Hall@insel.ch or Ralph.Schmid@insel.ch

Conflict of Interest: All authors declare no conflict of interest

Abbreviation list: human lung; mesenchymal; congenital lung malformations; CD90; vasculogenesis

Funding: LW is a doctoral student supported by a 4-year China Scholarship Council award. Laser scanning microscopy imaging was funded by the R'Equip grant from the Swiss National Science Foundation Nr. 316030_145003.

Running Title: CD90+CD146+ mesenchymal cells in human postnatal lung.

Background: Our understanding of mesenchymal cell subsets and their function in human lung affected by aging and in certain disease settings remain poorly described.

Methods: We use a combination of flow cytometry, prospective cell-sorting strategies, confocal imaging, and modeling of microvessel formation using advanced microfluidic chip technology to characterize mesenchymal cell subtypes in human postnatal and adult lung. Tissue was obtained from patients undergoing elective surgery for congenital pulmonary airway malformations (CPAM) and other airway abnormalities including chronic obstructive pulmonary disease (COPD).

Results: In microscopically normal postnatal human lung, there was a 5-fold higher mesenchymal compared with epithelial (EpCAM⁺) fraction, which diminished with age. The mesenchymal fraction composed of CD90⁺ and CD90⁺CD73⁺ cells were enriched in CXCL12 and PDGFR α and located in close proximity to EpCAM⁺ cells in the alveolar region. Surprisingly, alveolar organoids generated from EpCAM⁺ cells supported by CD90⁺ subset were immature and displayed dysplastic features. In congenital lung lesions, cystic airspaces and dysplastic alveolar regions were marked with an underlying thick interstitium composed of CD90⁺ and CD90⁺PDGFR α ⁺ cells. In postnatal lung, a subset of CD90⁺ cells co-express the pericyte marker CD146 and support self-assembly of perfusable microvessels. CD90⁺CD146⁺ cells from COPD patients fail to support microvessel formation due to fibrinolysis. Targeting the plasmin-plasminogen system during microvessel self-assembly prevented fibrin gel degradation but microvessels were narrower and excessive contraction blocked perfusion.

Conclusion: These data provide important new information regarding the immunophenotypic identity of key mesenchymal lineages and their change in diverse setting of congenital lung lesions and COPD.

INTRODUCTION

Injury to lung parenchyma from various insults induces a general wound healing response whereby damaged or lost epithelial cells are replaced with new ones resulting in restoration of tissue architecture and function (28). The regenerative process in response to acute injury is dependent upon not only activation of lung epithelial cells but also a pool of lung mesenchymal cells that ensure recapitulation of normal architecture during the regeneration phase. However, failure in this 2nd phase of wound repair due to persistent perturbations in resident mesenchymal cells has been postulated to account for the etiology of many chronic lung diseases (7). Fate mapping studies in murines have shed light on the cellular make-up of the lung mesenchymal compartment (33). An emerging body of evidence points toward lipid-body interstitial fibroblasts or lipofibroblasts, marked by platelet derived growth factor A (Pdgfra), being critical for both normal alveolar growth during development and proper regeneration after injury (4, 39, 62). This key mesenchymal progenitor cell can be enriched using fibroblast growth factor 10 (Fgf10), a pleiotropic molecule essential for regulating the growth of alveolar type II progenitor cells (16). However, these lipid-body Pdgfra⁺ interstitial fibroblasts also are a source of myofibroblasts, a key effector cell type in the pathogenesis of pulmonary fibrosis following bleomycin injury in murines (17, 60). However, the presence of lipofibroblasts in human lung has recently been called into question (1, 52). Therefore, despite the promising data generated from the preclinical studies in murines, the translational nature of these studies to humans is unknown (54).

Given the vast differences between murine and human lung with respect to development, architecture, cell composition and time scale of the repair response

following injury, there is an urgent need to assess the *in vivo* identity of mesenchymal lineages in diverse settings of lung injury in humans. It is of great clinical importance to characterize the cellular make-up of the mesenchymal compartment in human lung, to better understand the molecular mechanisms at work in certain disease settings that may represent an impediment to successful lung regeneration. This becomes increasingly more relevant as the use of cell-based therapies, some of which include non-resident mesenchymal cells, in the treatment of various lung disorders including idiopathic pulmonary fibrosis (IPF), emphysema and chronic obstructive pulmonary disease (COPD) increases (19, 21).

In the present study, we use a combination of polychromatic flow cytometric analysis, cell-isolation strategies, immunofluorescence analysis and microfluidic chip technology to identify and functionally characterize mesenchymal subtypes in postnatal human lung and their emergence in congenital lung disorders including congenital pulmonary airway malformations (CPAM) and other airway abnormalities. Furthermore, we compare our cellular findings with adult lungs of patients with COPD.

MATERIALS AND METHODS

Tissue samples and generation of single cells

Lung tissue was obtained from pediatric patients undergoing elective surgery for congenital pulmonary airway malformation (CPAM) and other various airway abnormalities at Children's University Hospital of Zurich (n = 19, age range: 5 days to 192 months, Table 1, neonatal (1/19), infancy (11/19), childhood (3/19), puberty (4/19)). Samples from the unaffected matched tissue shown microscopically to have a normal microarchitecture with small alveoli and bronchiole were used for RNA, flow cytometric analysis, cell isolation and histological analysis. Matched samples from the lung lesions were used for comparative histology. For comparison to adult lung, we obtained uninvolved lung tissue from patients diagnosed with COPD (n = 15, Supplemental Table S1, Digital identification object, DOI:[10.6084/m9.figshare.11799843](https://doi.org/10.6084/m9.figshare.11799843); URL <https://figshare.com/s/8da87d9d40436634c15e>) or without COPD (n = 15, Supplemental Table S2, DOI: [10.6084/m9.figshare.11799843](https://doi.org/10.6084/m9.figshare.11799843)) undergoing surgical resection because of a primary or secondary lung tumor at Bern University Hospital, Division of Thoracic Surgery. All patients gave informed written consent for usage of surgical material for research purposes, which was approved by Ethics Commission of the Canton of Bern (KEK-BE:042/2015). Generation of single cells suspension for flow cytometric analysis and prospective fluorescence-activated cell sorting (FACS) was performed as previously described (8). Briefly, mechanically disaggregated tissue was further disaggregated enzymatically using a solution containing animal free collagenases I and II (Worthington Biochemicals) at 0.1 and 0.25% respectively. Collagenase II and I were chosen due to their activities for collagenase, caseinase, clostripain, and tryptic activities. To prevent cells from clumping during tissue digestion and improve cell recovery, we included 0.2

mg/ml deoxyribonuclease I (Biochemicals) in the digestion buffer. Following digestion, single cell suspensions were used for FACS or cryofrozen and stored at -150°C for later use. For some patients, a small section of the tissue was immersed in cell recovery solution (Qiagen) and stored at -80°C for isolation of tissue RNA and RT-qPCR at a later time point.

Fluorescence-activated cell sorting and analysis

To prospectively isolate mesenchymal cell subsets, single cells were resuspended in staining buffer (2% FBS/1 mM EDTA/0.09% sodium azide) and following Fc block (eBioscience) incubated with a panel of fluorescently conjugated human monoclonal antibodies: CD45, CD14, CD31, CD73, CD90, EpCAM (see Supplemental Table S5, DOI: [10.6084/m9.figshare.11799843](https://doi.org/10.6084/m9.figshare.11799843)). Using a BD FACS Aria III or BD FACS Aria, cells were sorted directly into collection buffer containing 20% FBS (Gibco, Life Technologies). Cell boundaries requiring the proper placement of gates to sort prospective cell populations was determined using fluorescence minus one (FMO) strategy and an unstained control (25, 41). Doublets and debris were excluded based on FSC and SSC profiles and dead cells were excluded based on 7-AAD (Supplemental Fig. S1, DOI: [10.6084/m9.figshare.11799843](https://doi.org/10.6084/m9.figshare.11799843)). In a second cohort of lung tissue was obtained from postnatal (n = 6; PL017-PL022) and adult lungs (n = 6; patient 10-15, see Table S1, DOI: [10.6084/m9.figshare.11799843](https://doi.org/10.6084/m9.figshare.11799843)), we added the following monoclonal human antibodies CD146, NOTCH3 and integrin β_4 (CD104) (see Table S5, DOI: [10.6084/m9.figshare.11799843](https://doi.org/10.6084/m9.figshare.11799843)) to our original antibody panel to further discriminate the cell populations of interest.

Primary mesenchymal cell culture

FACS-sorted mesenchymal cell subsets were plated on regular tissue culture plastic precoated with 0.2% gelation solution (Sigma). Cells were expanded in chemically defined growth medium consisting of α MEM with ribonucleosides (Sigma) supplemented with 1% FBS, 200 mM L-glutamine (Gibco), 10 ng/mL of recombinant human fibroblast growth factor 2 (FGF2, Life Technologies), 20 ng/ml of recombinant human epidermal growth factor (EGF, Life Technologies), human insulin (1 mg/ml, Sigma). Media was formulated with antibiotic-antimycotic solution containing 10,000 units/mL of penicillin, 10,000 μ g/mL of streptomycin, and 25 μ g/mL of Amphotericin B (Gibco). Cells were maintained in a humidified 37°C low oxygen (3% O₂) incubator in 5% CO₂ until reaching confluence. On day 6 after plating, the medium was carefully aspirated and replaced with fresh medium and regular media changes were performed biweekly.

Histological and immunofluorescence analysis

From donor human postnatal lung tissue (n = 8; PL003, PL004, PL006, PL008, PL012, PL013, PL014, PL019, see Table 1 for patient information), formalin-fixed tissue was dehydrated in a series of increasing ethanol concentrations and embedded in paraffin. 5 μ m sections were stained with a panel of human monoclonal antibodies targeting EpCAM, CD73, CD90, SPC and PDGFR α (see Supplemental Table S6, DOI: [10.6084/m9.figshare.11799843](https://doi.org/10.6084/m9.figshare.11799843)). For antigen retrieval, slides were immersed in citrate buffer (10 mM, pH 5.5) and heated in a microwave. Following this, samples were washed 3X in TBS buffer. For blocking non-specific binding, slides were incubated for 30 min at room temperature in blocking solution (3% goat serum, 0.5% casein, 0.1% NaN₃ in TBS buffer). Following this, primary antibodies were diluted in the same blocking

solution and applied in 100 µl aliquots per slide, covered with paraffin film and incubated overnight in a humidified chamber at 4°C. Slides were washed 3X in TBS + 0.1% Tween 20 and secondary antibodies (see Supplemental Table 7, DOI: [10.6084/m9.figshare.11799843](https://doi.org/10.6084/m9.figshare.11799843)) diluted in TBS + 0.1% Tween 20 + 0.1% Tween 20 were applied in 100 µl aliquots to the slides and incubated for 3 hours in a humidified chamber at room temperature. Following this, all slides were washed 2X in TBS + 0.1% Tween 20. To counterstain nuclei, 100 µl of 4',6-diamidino-2-phenylindol (DAPI) (Molecular Probes, Invitrogen) solution was applied per slide for 30 seconds and washed for 5 min in TBS + 0.1% Tween 20. Slides were covered with EMS Shield Mount with antifading agent DABCO™ (Electron Microscopy Sciences) and edges sealed and slides kept in dark at 4°C prior to confocal microscopy. High resolution images were acquired with a Zeiss LSM 710 Confocal Microscope using the Zen software program (Zeiss). Images were collected as lsm files and imported into Imaris software Ver 7.6 (Bitplane, CH).

RNA extraction and real time quantitative PCR

Total RNA was extracted from lung tissue and all mesenchymal cell subsets using RNeasy Mini Kit (Qiagen) to analyze gene expression using real time quantitative PCR (RT-qPCR). RT-qPCR was performed in triplicates with target-specific primers using TaqMan Gene Expression Assay (Applied Biosystems) or dye-based detection with GoTaq PCR master mix (Promega) on AB7500 FAST real-time PCR system (Applied Biosystems). Expression levels were normalized to 3 internal controls tested for expression stability across samples in each experiment using Expression Suite Software (Life Technologies). Relative expression was calculated by $2^{-\Delta\Delta CT}$ method. (Table S3-4

for complete primer list, DOI:110.6084/m9.figshare.11799843). For relative gene expression of the mesenchymal compartment, IMR-90 normal human fetal lung fibroblasts (Coriell Cell Repository, Camden, NJ) or normal human lung fibroblasts (ATCC® CCL-204™) and set to one.

Mesenchymal differentiation

For adipogenic induction, postnatal lung-derived CD90⁺ and CD90⁺CD73⁺ cells (P3-P4), as well as CD90⁺CD73⁺ cells from the bone marrow of a healthy adult were plated per well in a 6-well dish in regular culture medium and placed in a humidified chamber with 5% CO₂ at 37°C. After 24 hours, the wells were washed with PBS and fresh adipogenic maintenance medium consisting of DMEM/Low glucose (Gibco), 10 µg/mL human insulin (Invitrogen), 10% FBS, 1% Penicillin/Streptomycin was added. After 3 days, the medium was changed to an adipogenic induction (Gibco, ThermoFisher Scientific). Fresh media changes were made every 3 days up to 21 days. At day 21, cells were fixed with 4% paraformaldehyde and stained with Oil Red O (Sigma) to detect formation of lipid droplets (23). In separate wells, RLT lysis buffer (Qiagen) was added and cell lysis stored at -80°C for generation of RNA at a later time point. For osteogenic induction, cells were plated in a 6-well dish in DMEM supplemented with 10% FBS and 1% Penicillin/Streptomycin. After 24 hours, media was changed and converted to osteogenic induction media (Gibco, ThermoFisher Scientific). Half-media changes were made every 3 days for a total of 21 days. At day 21, cells were fixed in 10% formalin and stained with 2 mM Alizarin Red S solution to detect extracellular calcium deposition. In separate wells, RLT lysis buffer (Qiagen) was added and cell lysis stored at -80°C for generation of RNA at a later time point. For chondrogenesis assay, early passage (P3-

P4) 5×10^5 CD90⁺CD73⁺ and CD90⁺CD73⁻ cells from postnatal lung were aliquot into 15ml conical tubes and centrifuged at 300g for 5 minutes. Afterwards, media was removed and replaced with 500µl of chondrogenic induction media (Lonza, Switzerland). After 21 days, micromass pellets were fixed with 70% ethanol for 30 minutes and washed in PBS. Pellets were embedded in GMA (Technovit 8100, Kuzler, Wehrheim, Germany) according to manufacturer's protocol. Sections of 4 µm thickness were cut with a Reichert-Jung with a "C" knife blade and were mounted on a glass slide. A. Toluidine blue staining was performed using the following recipe. Natrium-Tetrabora. Toluidine blue 1g dissolved in 100 ml of milliQ water and filtered to remove any particulate. Toluidine solution was diluted 1:1 with milliQ water and applied to slides for 3 min. Following staining, slides were washed 2 x 15 sec in 50% ethanol. Sections were allowed to air dry at room temperature and embedded in Eukitt. Micrographs were captured for each pellet using an Olympus BX50 microscope with a UPLAN FI objective 10x magnification. For comparison, we included MSCs isolated from adipose tissue and bone marrow from healthy adults.

Immunophenotype of cell subsets using flow cytometry

Following expansion, mesenchymal cell subsets were harvested and re-suspended in FACS staining buffer. Following Fc block, cells were incubated with the following fluorescently conjugated human monoclonal antibodies used to detect mesenchymal lineages (see Table S5, DOI:110.6084/m9.figshare.11799843). Cells were incubated on ice in the dark for 30 minutes. To exclude dead cells and debris, 7-AAD was added. Cell acquisition was performed using a BD FACS LSRII SORP. For analysis, a minimum

1x10⁴ events were collected and analyzed using FlowJo software version 10.7 (Tree Star).

Virosome and liposome uptake

Generation and characterization of influenza virosome and liposome formulations have been previously described (9). Briefly, Influenza virosomes were prepared as follows. In short: per ml of final formulation, 8 mg of DOPC (1,2-dioleoyl-sn-glycero-3-phosphocholine; Merck, Darmstadt, Germany) and 1 mg of OPPE were dissolved in 100 mM OEG in PBS pH 7.4 (52.7 mM phosphate, 82 mM NaCl). Inactivated Influenza A/Brisbane/59/2007 H1N1 virus was mixed with PBS and centrifuged for 1h at 18°C. The pellet of inactivated influenza virus was resuspended with 100 mM OEG-PBS pH 7.4 for 10 min followed by sonication for 1 min at 30°C. This mixture was centrifuged for 1h at 18°C to pellet down the nucleocapsid complex. The supernatant containing the solubilized influenza membrane proteins and lipids was used for virosome formulation and mixed with phospholipids at a concentration of 0.2 mg/ml hemagglutinin (HA). Virosome formation took place after removal of OEG detergent using 0.375 g per ml of formulation of SM2 Bio-Beads (BioRad) twice for 1 h and once for 30 min at room temperature whilst mixing at 100 rpm. Fluorescent virosomes were obtained by adding Atto647-PE as indicated prior to detergent removal to enable peptide incorporation. Liposomes were prepared similarly by leaving out the influenza virus component but following the same procedure. At the end of the process virosomes and liposomes were sterile filtered on 0.22 µm units (Millex-GP; Merck Millipore). To study uptake of influenza virosomes and liposomes, 10⁵ mesenchymal cells from matched lung tissue were seeded per well in a six well dish (Corning). After 48 hours, cells were incubated

with influenza virosome particles (5 µg HA), liposome particles or PBS (vehicle control) for 18h. Uptake of nanoparticles was determined by measuring Atto-AF647 signal by flow cytometry (LSRII SORP, BD Biosciences). Data was analyzed using FlowJo V10 (TreeStar, Ashland, OR, USA) software. A minimum of 1×10^4 events were collected.

H1N1 influenza viral infection

Influenza virus H1N1 A/PR/8/32 (ATTC, VR-1469) was propagated in MDCK II cell line (ATCC, CRL-2936) and virus titers were assessed with a TCID₅₀ assay using a crystal violet stain. To evaluate the susceptibility of postnatal lung-derived CD90⁺CD146⁺ mesenchymal cells towards influenza virus infection we used a flow cytometry approach. CD90⁺CD146⁺ mesenchymal cells were infected at a multiplicity of infection of 1 TCID₅₀/cell in serum-free medium supplemented with acetylated trypsin from bovine pancreas (Sigma, T6763) during 1h in a humidified 5% CO₂ incubator at 37°C. Next, the cells were harvested 16, 24 and 48h post-infection and stained intracellularly with a mouse anti-influenza nuclear protein (NP) antibody (ATCC, HB-65, clone H16-L10-4R5). N = 3, biological replicates. Data were acquired on a Canto flow cytometer (BD Bioscience) and analysed with the FlowJo ver10 software (Tree Star). Supernatants were collected and stored at -20°C until further analysis by the TCID₅₀ assay.

Vasculogenesis-on-chip

The microfluidic device, chip fabrication process, cell seeding, chip maintenance, immunostaining and permeability assay have been previously described in detail [1], [2]. Briefly, HUVECs and postnatal- or COPD-derived CD90⁺CD146⁺ mesenchymal cells were suspended in 2 U/ml bovine plasma thrombin (Sigma) in endothelial basal medium 2 (EBM2; Lonza) at final concentrations of 2×10^7 and 1×10^7 cells/ml, respectively. For

cell seeding, first, HUVECs, CD90⁺CD146⁺ cells, and fibrinogen solution were mixed at a ratio of 1:1:2 and immediately seeded into the central chamber. Next, a 1:1 mixture of CD90⁺CD146⁺ cells and fibrinogen solution was immediately loaded in the side chambers. After 10 min, EGM2 was loaded in microchannels and the reservoirs were filled. All chips were incubated for 7 days. The experiments were carried out from three different postnatal and COPD-derived biological donors. After 7 days of co-culturing, some of the chips were fixed for immunostaining against PECAM-1, α SMA, F-actin and DAPI. The remaining chips were used for perfusion assay with 70 kDa RITC-dextran in live vessels. In separate experiments, HUVECs and CD90⁺CD146⁺ cells from postnatal or COPD patients were seeded in fibrin gels within the microfluidic device, as described above. To examine the impact of antifibrinolytic agent epsilon-Aminocaproic acid (EACA) (Sigma) on vessel formation, EACA was added to the cell culture medium at a final concentration of 200 μ g/ml. EACA-EBM2 medium was used in the microfluidic device for coculturing HUVECs and CD90⁺CD146⁺ cells starting from day 0 until day 6. After 7 days of culturing in the presence of EACA, chips were prepared for immunostaining or for perfusion measurements, as described above.

T-cell activation assay

Peripheral blood mononuclear cells (MNCs) were isolated from healthy blood bank donors using Ficoll-PaqueTM Plus (GE Healthcare Life Sciences, Switzerland) density gradient centrifugation. Following this, highly purified CD3⁺ T cells were isolated from the MNC pellet using the EasySepTM Human T Cell Isolation Kit (StemCell Technologies) according to the manufacturer's instructions. Healthy donor T cells were labeled with 0.5 μ M CFSE (eBioscience) according to the manufacturer's instructions. CFSE-labeled

CD3⁺ T cells (2×10^5) were stimulated with CD3/CD28/CD2 activator beads (Stemcell Technologies) in 96-wells U-bottom plates in T cell media (Immunocult XF, StemCell Technologies) supplemented with 10 ng/ml of recombinant human IL-2 (Peprotech) at 37°C and 5% CO₂. Separately, mesenchymal cell subsets were gamma irradiated (10 Gy) and in separate wells, 4×10^4 , 2×10^5 or cells were added to wells containing 2×10^5 CFSE-labeled T cells activated with CD3/CD28/CD2 activator beads. Following this, co-cultures were treated with 50 ng/ml of rhTNF α (Gibco) and 50 ng/ml of rhIFN γ (Gibco) or vehicle. After 5 days of culture at 37°C and 5% CO₂, cell-free supernatant was collected, frozen and stored at -20°C for later analysis. Cells were harvested and were stained with a cocktail of antibodies: anti-human CD45, anti-human CD4 and anti-human CD8 (see e-Table 5). Cell viability was determined using 7-AAD (eBioscience) according to the manufacturer's protocol. Cells were analyzed for proliferation using CFSE-dilution patterns and for phenotype on a BD LSRII SORP(BD Biosciences). For analysis of phenotypic markers, we used FlowJo software ver 10.1 (TreeStar) and precursor frequencies of activated CD4⁺ and CD8⁺ T cells were calculated. A minimum of 1×10^5 events were collected for analysis.

Metformin treatment

Early passage CD90⁺CD146⁺ cells from surgically resected early postnatal lung or COPD lung tissue were seeded at 1×10^5 cells per well in regular culture media. After 24 hours, cells were growth arrested by replacing regular culture media with serum free media. After 24 hours, cells were treated with 5 ng/mL of recombinant human TGF β 1 (Gibco) without or with 0.5mM metformin (StemCell Technologies) over 72 hours. TGF β 1 and metformin were refreshed at each media change. After 72 hours, RLT lysis

buffer was added to each well and cell lysates were stored at -80°C for generation of RNA at a later time point. In separate experiments, early passage CD90⁺CD146⁺ mesenchymal cells from postnatal lung or COPD lung tissue, as well as MSCs from bone marrow and adipose tissue (CellnTec, Bern Switzerland) were seeded at 2 x 10⁵ cells per well in a 6-well dish in regular culture medium. After 24 hours, cells were converted to adipogenic induction media (Gibco), as described above, without or with 0.5 mM metformin. Fresh media changes were made every 3 days up to 21 days. Metformin was added at each media change. At day 21, RLT lysis buffer (Qiagen) was added and cell lysis stored at -80°C for generation of RNA at a later time point.

Statistical analysis

Data are expressed as mean ± SD. Comparisons between two groups were carried out using the parametric student's two-tailed paired or unpaired t-test for normally distributed data. If data were not distributed normally, a nonparametric Wilcoxon signed-rank test was used between the two groups. One-way analysis of variance (ANOVA) followed by Newman-Keuls post hoc test was used for analysis of more than two groups. The numbers of samples (biological replicates) per group (n), or the numbers of experiments (technical replicates) are specified in the figure legends. To test whether there was a correlation between age and mesenchymal and epithelial compartments, Pearson's correlation coefficient was used, assuming a normal distribution of the data. Data was analyzed using GraphPad Prism 8 software. Statistical significance is accepted at P<0.05.

RESULTS

Cellular identification of mesenchymal subsets in human postnatal lung

We set out to identify and characterize mesenchymal lineages in postnatal lung tissue obtained from pediatric patients undergoing elective surgery for congenital lung lesions and other airway abnormalities (Figure 1A, see Supplemental Table 1 and Fig. S1, DOI: [10.6084/m9.figshare.11799843](https://doi.org/10.6084/m9.figshare.11799843)). Flow cytometric analysis of unaffected resected lung tissue determined microscopically to have normal microarchitecture with small alveoli and bronchiole revealed a prominent mesenchymal fraction based on the marker profile EpCAM⁻CD45⁻CD31⁻CD14⁻ (gate R4, referred to as EpCAM⁻), as shown in the representative bivariate flow cytometric plot in Figure 1B (Supplemental Fig. S2 for full gating strategy, DOI: [10.6084/m9.figshare.11799843](https://doi.org/10.6084/m9.figshare.11799843)). Interestingly, the EpCAM⁻ fraction was 4.8 fold higher compared to EpCAM⁺ fraction (EpCAM⁻, 24.2±15% versus EpCAM⁺, 5.01±2.8%, respectively, Figure 1C). With age the EpCAM⁻ fraction declined significantly (Figure 1D). The decline in the EpCAM⁻ was confirmed in adult human lung (Figure 1E and Supplemental Fig. S3A-E, DOI: [10.6084/m9.figshare.11799843](https://doi.org/10.6084/m9.figshare.11799843)). In adult human lung, the EpCAM⁻ fraction was 2.3±2.4% of live cells compared to 6.8±4.2% for the EpCAM⁺ fraction (Figure 1F and Supplemental Fig. S3A-E, DOI: [10.6084/m9.figshare.11799843](https://doi.org/10.6084/m9.figshare.11799843)). We further characterized the EpCAM⁻ fraction based on marker expression of 5'ecto-nucleotidase CD73 (NT5E) and membrane glycoprotein CD90 (THY-1), strong candidate markers for the direct identification of multipotent mesenchymal cells within various human tissues (12). As shown in a representative bivariate plot (Figure 1G), single CD90⁺ cells are the predominate cell subset (34.7±19.2%) followed by CD90⁺CD73⁺ (15.8±19%), whereas single CD73⁺ (1.5±1.3) cells were rare (Figure 1H). Interestingly, the % of these fractions change with age

(Figure I, J), whereby the majority of cells switch from CD90⁺CD73⁻ to CD73⁺ with or without CD90⁺ adult lung (Supplemental Fig. S3F, DOI: [10.6084/m9.figshare.11799843](https://doi.org/10.6084/m9.figshare.11799843)). Next, we sought to visualize the anatomical localization of CD90⁺ subsets in human postnatal lung tissue. Standard H&E staining of microscopically normal postnatal lung tissue demonstrate a normal alveolar region (Figure 1K). Immunofluorescence (IF) staining and confocal microscopy show single CD90⁺ cells, as well as CD90⁺CD73⁺ cells in close proximity to EpCAM⁺ cells in the alveolar region (Figure 1L). These data show that the pulmonary mesenchyme, although often overlooked, represents a major cellular constituent in early postnatal human lung that dramatically declines with aging.

Postnatal lung CD90⁺ mesenchymal cells enriched in niche factors PDGFR α and CXCL12 yet possess diminished adipogenic differentiation capacity

FACS analysis shows that there are two distinct CD90⁺ populations based on CD73 expression. FACS-purified CD90⁺CD73⁺ and CD90⁺CD73⁻ subsets were expanded using a chemically defined media for mesenchymal cells (Figure 2A and Supplemental Table S8, DOI: [10.6084/m9.figshare.11799843](https://doi.org/10.6084/m9.figshare.11799843)). Morphologically, both subsets appear pericyte-like comprised of a central nucleus with small, finger-like branches (Figure 2B). Characterization of these two subsets show higher mRNA levels of CXCL12 and PDGFR α , key niche factors shown to contribute to alveolar development and regeneration in murine lungs, in both CD90⁺CD73⁻ and CD90⁺CD73⁺ cells compared to lung tissue (Supplemental Fig. S4A, DOI: [10.6084/m9.figshare.11799843](https://doi.org/10.6084/m9.figshare.11799843)) (4, 45). Expression of FGF10 and IL-6, important morphogens in lung development in mice (16) and leptin receptor (LEPR), which marks a subset of bone marrow-derived MSCs also in mice (22), were reduced in CD90⁺CD73⁻ and CD90⁺CD73⁺ cells compared to lung

tissue. Although the expression level of GLI1, a zinc finger protein marking mesenchymal cells with a pericyte/mesenchymal stem cell (MSC) origin in mice (29), was elevated in both CD90⁺CD73⁻ and CD90⁺CD73⁺ cells compared with human lung embryonic fibroblasts, neither population were enriched in common pericyte markers RGS5 and desmin; nor makers of differentiated cell types α SMA (ACT2) and calponin (CNN1). There were no difference in the expression of other mesenchymal markers shown to be important for early lung development such as WNT5A, FGFR1, beta-catenin and NOGGIN compared with tissue (data not shown). Since CD90 and CD73 are critical markers used to define mesenchymal stem/stromal cells (MSCs), we characterized the mesenchymal differentiation potential of the CD90⁺ subsets. Despite both CD90⁺CD73⁻ and CD90⁺CD73⁺ cells being enriched in PDGFR α , neutral lipid formation was diminished compared with CD90⁺CD73⁺ MSCs from human bone marrow (BM) of healthy adults (23). By contrast, the osteogenic potential of both subsets is comparable to BM-derived CD90⁺CD73⁺ MSCs (Figure 2D). Finally, using a micromass pellet assay, the chondrogenic differentiation potential of CD90⁺CD73⁺ and CD90⁺CD73⁻ subsets was similar to BM-derived CD90⁺CD73⁺ MSCs and adipose tissue-derived MSCs based on Toluidine blue staining (Figure 2E-F).

CD90⁺ and CD90⁺PDGFR α ⁺ mesenchymal cells fill thickened interstitial spaces in airway and dysplastic alveolar epithelium

Recent work in murines demonstrate distinct mesenchymal lineages promote epithelial renewal and myofibrogenesis following injury (62). To investigate this, we developed an alveolar organoid system (4). We seeded CD90⁺ mesenchymal cells with autologous EpCAM⁺CD73⁺ epithelial stem/progenitor cells FACS-purified from postnatal human lung

444 in matrigel (Figure 3A). Three weeks after differentiation in alveolar induction media,
445 organoid structures expressing E-cadherin⁺ (green) were surrounded by PDGFR α ⁺
446 mesenchymal cells (Figure 3B). In microscopically normal alveolar region of postnatal
447 lung, CD90⁺ cells co-expressing PDGFR α can be observed, although very few (Figure
448 3C). Significant overexpression of key transcription factors SOX2, SOX9 and TP63
449 along with KRT5 was observed in organoid structures compared to native lung tissue
450 suggestive that organoid structures are dysplastic. To determine whether CD90⁺ subset
451 become activated after injury, we performed histological and IF staining of lung lesions
452 resected from patients diagnosed with CPAM and other airway abnormalities. Standard
453 H&E and IF staining of lung sections obtained from microscopically normal postnatal
454 lung tissue show normal airway and alveolar regions (Supplemental Fig. S5A-C, DOI:
455 [10.6084/m9.figshare.11799843](https://doi.org/10.6084/m9.figshare.11799843)). By comparison, H&E staining of matched lesions
456 resected from CPAM tissues from two patients with concomitant respiratory infection
457 show significant areas of macrocystic and microcystic airway and alveolar lesions
458 (Figure 3E, H and Supplemental Fig. S1B-C, DOI: [10.6084/m9.figshare.11799843](https://doi.org/10.6084/m9.figshare.11799843)). In
459 the patient with CPAM/chronic infection, IF staining shows thickened airway interstitium
460 filled with CD90⁺ cells, some of which also co-stain for PDGFR α (Figure 3F-G). In the
461 patient with CPAM/RSV infection, a greater abundance of CD90⁺ cells co-staining for
462 PDGFR α was observed in the alveolar region (Figure 3I-J). Comparable histological
463 observations were noted in a third patient with chronic bronchiolitis, whereby cystic
464 airspaces lined with a simple layer of cuboidal EpCAM⁺ cells contained an underlying
465 extensive network of CD90⁺ mesenchymal cells, some co-staining for PDGFR α (Figure
466 3K-M). In this same patient, we noted significant expansion of CD90⁺PDGFR α ⁺
467 mesenchymal cells underlying thickened airway lining (Supplemental Fig. S5D-F, DOI:

[10.6084/m9.figshare.11799843](https://doi.org/10.6084/m9.figshare.11799843)), as well as in the dysplastic alveolar region (Supplemental Fig. S5G-I, DOI: [10.6084/m9.figshare.11799843](https://doi.org/10.6084/m9.figshare.11799843)). Finally, in lungs of a patient with lobar emphysema, we also note dysplastic alveolar regions marked by expanded CD90⁺ cells where some co-stain for PDGFR α (Supplemental Fig. S5J-L, DOI: [10.6084/m9.figshare.11799843](https://doi.org/10.6084/m9.figshare.11799843)). Taken together, these data show that congenital lung lesions exhibit a pronounced expansion in mesenchymal cells. The contribution of CD90⁺ mesenchymal cells to disease etiology and pathogenesis of congenital lung lesions warrants further investigation.

Influenza A virus infects and replicates in postnatal lung CD90⁺CD146⁺ mesenchymal cells

Based on their anatomical location in the alveolus, we hypothesized that CD90⁺ subsets may contain pericytes, as previously shown at the ultrastructural level (57). FACS analysis shows that 21.9 \pm 16.9% of CD90⁺CD73⁻ and 5.4 \pm 4.4% of CD90⁺CD73⁺ cells express the pericyte marker CD146 but not NOTCH3 (Figure 4A-B). At the surface level, CD90⁺CD73⁻CD146⁺ cells expressed higher levels of PDGFR β , CD166 and podoplanin (PDPN) compared with CD90⁺CD73⁻CD146⁻ cells (Figure 4C). CD146⁺ pericytes are essential for tissue repair following injury by participating in vasculogenesis (12) and regulation of host immune system (6). Recently, the use of virosomes and liposomes as nanocarriers to deliver cargo to lung tissue in a cell type specific manner has been described (9). While influenza virosomes target specific immune and parenchymal cell types of the respiratory tract, less is known regarding their interaction with nonparenchymal mesenchymal cell types. To test this, we exposed postnatal lung-derived CD90⁺CD73⁻CD146⁺ mesenchymal cells to liposomes or influenza virosomes

492 conjugated to the fluorochrome Atto647 (Figure 4D). FACS analysis shows a greater
493 uptake of influenza virosomes compared with liposomes by CD90⁺CD73⁻CD146⁺ (Figure
494 4D). Interestingly, H1N1 influenza virosome (Brisbane A strain) demonstrated the
495 greatest tropism, whereas H3N2 (Texas strain) showed the lowest tropism (Figure 4E).
496 Virosome uptake did not induce changes in cell surface expression of intercellular
497 adhesion molecule 1 (ICAM1, CD54) nor the HLA major histocompatibility complex,
498 class II, DR Alpha (HLA-DRA) (data not shown). To determine whether CD90⁺CD73⁻
499 CD146⁺ mesenchymal cells also represent a target for viral tropism, we infected cells
500 with live H1N1 influenza virus (PR8 strain). FACS analysis shows influenza nuclear
501 protein (NP) expression at 16, 24 and 48 hours post-infection demonstrating H1N1 was
502 capable of infecting postnatal lung-derived CD90⁺CD73⁻CD146⁺ cells compared to mock
503 infected cells (Figure 4F-H). Culture supernatants isolated from H1N1 infected
504 CD90⁺CD73⁻CD146⁺ mesenchymal cells as early as 8 hours post infection and up until
505 48 hours post infection demonstrate that H1N1 actively replicates inside infected cells
506 (Figure 4I). To further address immune modulation of mesenchymal subsets, we tested
507 whether CD90⁺CD73⁻CD146⁺ and CD90⁺CD73⁻CD146⁻ mesenchymal cells block that
508 activation of T cells. For this, we cultured both mesenchymal cell subsets in the
509 presence of carboxyfluorescein succinimidyl ester (CFSE-)-labelled CD3⁺ T cells derived
510 from peripheral blood mononuclear cells of healthy donors stimulated with
511 CD3/CD28/CD2 T cell activator beads (Supplemental Fig. S6A, DOI:
512 [10.6084/m9.figshare.11799843](https://doi.org/10.6084/m9.figshare.11799843)). Both postnatal CD90⁺CD73⁻CD146⁺ and CD90⁺CD73⁻
513 CD146⁻ mesenchymal cells were able to arrest activation of healthy CD4⁺ and CD8⁺ T
514 cells in a dose-dependent manner (Supplemental Fig. S6B-F, DOI:
515 [10.6084/m9.figshare.11799843](https://doi.org/10.6084/m9.figshare.11799843)). This was also confirmed with CD4 and CD8 T cells

isolated from human lung activated using staphylococcus enterotoxin B (Supplemental Fig. S6G-H, DOI: [10.6084/m9.figshare.11799843](https://doi.org/10.6084/m9.figshare.11799843)). Taken together, these data underscore the dynamic nature CD90⁺CD146⁺ mesenchymal cells in postnatal human lung being equipped to function as immune sensing cells able to respond to changes in the pulmonary microenvironment.

CD90⁺CD146⁺ mesenchymal subset is maintained in COPD

FACS analysis shows that the mesenchymal fraction diminishes with age. In chronic lung disease associated with fibrosis, there is evidence of an important role of the mesenchymal compartment (6, 33). Whether this also is the case in chronic obstructive pulmonary disease (COPD) is unknown. To investigate this, we performed flow cytometric analysis on uninvolved regions of surgically resected tissue obtained from lung cancer patients diagnosed with COPD according to GOLD guidelines. FACS analysis shows there was an increase in the EpCAM⁺ mesenchymal fraction (Figure 5A) in COPD compared with non-COPD resected lung tissue (COPD, 11.7±15 versus non-COPD, 2.3±2.4%, p<0.0051) (Figure 5B). This coincides with an increase in EpCAM⁺/EpCAM⁺ ratio in COPD compared with non-COPD controls (COPD, 4.9±12% and non-COPD, 0.41±0.3%, respectively) (Figure 5C). The distribution of mesenchymal subtypes based on subgating for CD90 and CD73 was not altered in COPD (Figure 5D). Surprisingly, CD146 expression in CD90 and CD73 subsets increased in COPD compared with non-COPD controls (Figure 5E). FACS-purified CD90⁺CD146⁺ cells from COPD patients shows a distinct myogenic-like morphology (Figure 5F) and downregulate the expression of GLI1, PDPN and the lung morphogen FGF10 (Figure 5G). Decreased levels of angiopoietin 1 (ANGPT1), which is critical for normal vascular

development, also were found in CD90⁺CD146⁺ cells in COPD (Figure 5G). Recently it was shown that first-line antidiabetic drug metformin inhibits the fibrotic effects of TGFβ1 on human lung fibroblasts while inducing lipogenic differentiation (27). When exposed to TGFβ1, CD90⁺CD146⁺ cells from COPD upregulated expression of fibroblast activation protein alpha (FAP) and collagen 1A1, which was not blocked by metformin (Figure 5H). In addition, CD90⁺CD146⁺ cells from COPD or postnatal lung tissue lack adipogenic potential and metformin treatment had no effect on the lack of adipogenesis (Supplemental Fig. S7, DOI: [10.6084/m9.figshare.11799843](https://doi.org/10.6084/m9.figshare.11799843)). In addition, metformin did not enhance adipogenesis in control BM- or adipose-derived MSCs.

CD90⁺CD146⁺ mesenchymal cells in COPD fail to support microvessel formation

Injury to the lung impairs the function of different subsets of tissue resident mesenchymal cells (10, 11). In COPD, there is evidence of vascular dysfunction not explained by defects in the vascular endothelium (35). Using a three dimensional (3D) microfluidic device, we next asked whether CD90⁺CD146⁺ cells support microvessel formation *de novo* and whether this function is impaired in COPD (Figure 6A-B) (61). Imaging of the central chamber of the microfluidic device shows that postnatal CD90⁺CD146⁺ cells support self-assembly of 3D networks consisting of lumen-forming HUVECs stained with the pan-endothelial marker CD31 (circular image, Figure 6C). By contrast, CD90⁺CD146⁺ cells from COPD fail to support 3D vascular network formation (Figure 6D). Serial images of vascular network in the central chamber supported by postnatal CD90⁺CD146⁺ cells shows communication between CD31⁺ HUVECs (red) with αSMA⁺ pericyte-like cells (green) located on the abluminal surface (Figure 6E). An orthogonal view of merged images shows open lumens (Figure 6G). By contrast, COPD

564 CD90⁺CD146⁺ cells (αSMA, green) degrade the fibrin gel resulting in the formation of 2D
565 cell layer with CD31⁺ HUVECs (red) on the bottom of the microfluidic device within the
566 central chamber, shown as serial images (Figure 6F) with no evidence of lumen
567 formation (Figure 6H). Microvasculature structures supported by postnatal
568 CD90⁺CD146⁺ cells were perfusable confirmed following application of 70 kDa RITC-
569 dextran, attaining a permeability coefficient of $2.1 \pm 2 \times 10^{-4}$ cm/s (Figure 6I, left panels
570 and Supplemental Video S1, DOI: [10.6084/m9.figshare.11799843](https://doi.org/10.6084/m9.figshare.11799843)). Single postnatal
571 CD90⁺CD146⁺ cells within fibrin gel in the side chamber do not form lumens but rather
572 migrate towards the central chamber in support vessel self-assembly (Supplemental Fig.
573 S8A and Supplemental Video S2, DOI: [10.6084/m9.figshare.11799843](https://doi.org/10.6084/m9.figshare.11799843)). Three-
574 dimensional nature of the vascular structure formed in the central chamber was
575 illustrated following volume rendering (Supplemental Fig. S8A, DOI:
576 [10.6084/m9.figshare.11799843](https://doi.org/10.6084/m9.figshare.11799843)). By contrast, structures supported by COPD
577 CD90⁺CD146⁺ cells were not perfusable (Figure 6I, right panels and Supplemental
578 Video S1, DOI: [10.6084/m9.figshare.11799843](https://doi.org/10.6084/m9.figshare.11799843)), as well, cells in the side chamber also
579 degrade the fibrin gel and fail to migrate (Supplemental Fig. S8B, and Supplemental
580 Video S2, DOI: [10.6084/m9.figshare.11799843](https://doi.org/10.6084/m9.figshare.11799843)). 3D volume rendering confirms the
581 single 2D layer formed in the central chamber (Supplemental Fig. S8B, DOI:
582 [10.6084/m9.figshare.11799843](https://doi.org/10.6084/m9.figshare.11799843)). To further address fibrinolysis in COPD cells, we
583 treated cocultures with the antifibrinolytic lysine analogue epsilon-aminocaproic acid
584 (EACA), which inhibits the conversion of plasminogen to plasmin. Targeting of the
585 plasmin-plasminogen system with EACA did not prevent postnatal CD90⁺CD146⁺ cells
586 from supporting 3D vascular network formation (Figure 6J). Importantly, EACA
587 prevented COPD CD90⁺CD146⁺ cells from degrading the fibrin extracellular matrix

enabling the formation of microvessel-like structures (Figure 6K). Z-stack projection of merged channels from the central chamber shows open lumens (Figure 6L-M). The morphology of EACA treated COPD CD90⁺CD146⁺ cells in the fibrin gel in the side chamber was similar to their postnatal lung counterparts; however, αSMA was not detected in 3D vascular network generated from postnatal CD90⁺CD146⁺ cells (Supplemental Fig. S8C-D, DOI: [10.6084/m9.figshare.11799843](https://doi.org/10.6084/m9.figshare.11799843)). Microvessel-like structures formed with postnatal CD90⁺CD146⁺ cells in the presence of EACA were perfusable (Figure 6N); however, the permeability co-efficient increased by a factor of 3.5 ($7.01 \pm 6.92 \times 10^{-4}$ cm/s, n = 4). By contrast, microvessel-like structures supported by COPD CD90⁺CD146⁺ cells in the presence of EACA were not perfusable due to contraction of the fibrin gel (Figure 6N, right panels and Supplemental Fig. S8D-E, DOI: [10.6084/m9.figshare.11799843](https://doi.org/10.6084/m9.figshare.11799843)). Second, the microvessel-like structures that formed in the central chamber were narrower compared with CD90⁺CD146⁺ cells from postnatal lung (Figure 6O). This suggests that direct interaction with the ECM activate biochemical and mechanosensing cues unmasking the pathological phenotype of mesenchymal cells from COPD lungs. Collectively, CD90⁺CD146⁺ pericyte-like cells may represent a novel target in the pathogenesis of COPD.

DISCUSSION

In this study, we used flow cytometry to identify and quantify distinct mesenchymal lineages in human postnatal and adult lung. Single CD90⁺ cells and CD90⁺CD73⁺, the major mesenchymal cell types enriched in microscopically normal postnatal lung. The spatial proximity of CD90⁺ mesenchymal cells to EpCAM⁺ progenitor cells suggests they could function as niche-supporting cells in the alveolus. At the mRNA level, postnatal CD90⁺ subsets are enriched in PDGFR α . A loss of alveolar PDGFR α ⁺ mesenchymal cells is a signature feature in bronchopulmonary dysplasia (BPD) (43), a serious lung disease prevalent in preterm infants characterized by a reduction in gas exchange surface area due to oversimplified or diminished alveoli (34). Surprisingly, organoids generated in matrigel from single EpCAM⁺ progenitor cells supported by autologous CD90⁺ subsets from microscopically normal postnatal lung failed to recapitulate normal alveolar structures. Second, structures were dysplastic at the gene level (59). Although expressing PDGFR α , CD90⁺ subsets possess limited adipogenic potential when compared to FACS-purified CD90⁺CD73⁺ cells from human bone marrow (23). These findings are in contrast to murines where alveolar CD90⁺PDGFR α ⁺ lipid-laden lipofibroblasts in direct contact with ATII progenitor cells provide lipid and other critical paracrine factors necessary for normal alveolar development, as well as regeneration following injury (4, 62). Tcf21, a basic helix-loop-helix transcription factor, was used to identify cells with lipofibroblast potential (40). We did not determine whether CD90⁺ perivascular-like cells express Tcf21. Despite this, it will be important to investigate whether forced expression of Tcf21 induces a lipid formation in CD90⁺ perivascular-like cells in human lung. Immunostaining analysis of congenital lung lesions and other airway abnormalities revealed an unexpected expansion in CD90⁺ and CD90⁺PDGFR α ⁺

mesenchyme in thickened interstitial spaces between cysts, as well as dysplastic alveolar regions. Although mesenchymal spindle-shaped cells in CPAM lesions have been described using standard histological staining, their cellular identity and role in disease pathogenesis is not known (15, 42). Recently, Swarr and colleagues performed the first comprehensive transcriptome-wide analysis of various congenital lung lesions demonstrating dysregulated expression of genes related to RAS and PI3K/AKT/mTOR pathway, together with a cell-autonomous defect in the growth and airway differentiation of EpCAM⁺ progenitor cells (51). However, an involvement in lung mesenchyme was not described. Besides targeting epithelial wound healing, PI3K/mTOR pathway is upregulated in lung fibroblasts contributing to lung fibrosis following bleomycin injury (37). Whether PI3K/AKT/mTOR pathway also is at play in CD90⁺ and CD90⁺CD73⁺ mesenchymal cells contributing to disease pathogenesis in congenital lung lesions requires further investigation.

A fraction of cells within the CD90⁺ subsets expressed the common pericyte surface marker CD146 and was enriched in GLI1, a marker of perivascular progenitor cells (29). FACS-purified CD90⁺CD146⁺ cells from microscopically normal postnatal lung support the self-assembly of patent microvessels and possess immune regulatory function (26). In COPD, we noted an increase in the mesenchymal fraction, which coincided with an increase in CD90⁺CD146⁺ subset compared with adults without COPD. To date, the pathogenesis of COPD has primarily focused on defects in airway basal cells (13, 20, 50) and the immune system (5). However, various changes in the pulmonary vascular system also have been reported (30, 36). Increased levels of soluble CD146 in plasma and bronchioalveolar lavage (BALF) were found in smokers with COPD (31). The adhesion molecule CD146 provides support for the growing

654 vasculature, yet the vascular supportive function of CD90⁺CD146⁺ cells in COPD was
655 abolished due to extensive fibrinolysis. A deregulated fibroblast repair capacity may be
656 critically involved in the pathogenesis of emphysema (55). FACS-purified CD90⁺CD146⁺
657 cells were expanded on dishes coated with gelatin rather than a stiff plastic culture
658 substrate. Despite clear differences in their morphology on 2D plastic, surprisingly there
659 was no difference in the expression level of the myofibroblast marker α SMA between
660 postnatal and COPD CD90⁺CD146⁺ cells. We also did not detect any differences in
661 basal expression of enzymes involved in extracellular matrix degradation such as
662 MMP2, MMP9 and SERPINE2 (data not shown). There were clear differences in matrix
663 mechanosensing properties between postnatal and COPD CD90⁺CD146⁺ cells
664 suggesting that COPD-derived cells “sense” stiffness activating a fibrinolytic state.
665 Properties of the matrix play a critical role in determining cell fate (18). Fibrin gels are
666 mildly compliant. The Young modulus (mechanical stress per strain) of the fibrin network
667 is less than 1 kPa (14). This is similar to healthy lung tissue with a general stiffness of
668 around 2kPa (49). Targeting the plasmin-plasminogen system with the lysine analogue
669 EACA blocked COPD CD90⁺CD146⁺ cells from degrading fibrin gel thus enabling the
670 generation of 3D microvessel-like structures, although narrower compared with
671 CD90⁺CD146⁺ cells from postnatal lung. Despite this, the contractile property of COPD
672 CD90⁺CD146⁺ cells prevented perfusion. Therefore, direct interaction with the ECM
673 activate biochemical and mechanosensing cues in COPD CD90⁺CD146⁺ cells
674 unmasking their pathological state, which may go undetected in 2D culture systems.
675 Interestingly, human PDGFR- β positive pericytes derived from lungs of patients with
676 idiopathic pulmonary fibrosis (IPF) demonstrated similar features of increased
677 invasiveness and response to exposure to TGF β 1 (58).

Our study has several limitations. First, although our FACS panel enables us to properly discriminate and isolate mesenchymal cell subsets, it is limiting due to an inability to follow the trajectory of CD90⁺CD146⁺ subset during chronic lung injury. In rodents, exposure to high oxygen levels disrupts the dual immune regulating and vascular supportive function of neonatal-lung derived CD146⁺ mesenchymal stromal cells (11). Similar findings were recently reported for a population of CD146 positive mesenchyme cells purified from human fetal lung when exposed to high levels of oxygen (38). The data supports a local source of mesenchymal cells versus a circulating source from the bone marrow contributing to adverse remodeling following lung injury (10). Therefore, it is reasonable to conclude that the CD90⁺ population identified in our report, which contain a subpopulation positive for CD146 with immune regulatory properties (26), could be precursors to the cells found in tracheal aspirates of neonates following lung injury from bronchopulmonary dysplasia (BPD)(46). An unresolved question is whether MSC-like cells arise from a perivascular location in the bronchial vasculature or alveolar compartment found on small vessels (10, 44). Another limitation is the limited marker profile to prospectively identify cells with pericyte-like function. We found that the common lymphendothelial marker PDPN is highly upregulated on postnatal CD90⁺CD146⁺ cells. PDPN has been described to be expressed on a wide variety of cells including fibroblast reticular cells and type I lung epithelial cells (2). In murines, PDPN positive fibroblastic reticular cells co-expressing PDGFR β in lymph nodes are responsible for maintaining vascular integrity. Loss of PDPN leads to increased bleeding. PDPN-expressing arteriolar pericytes have been described in bone marrow of murines (53). At the mRNA level, PDPN is downregulated in CD90⁺CD146⁺ cells in COPD. Whether downregulation in PDPN contributes to the dysregulated perivascular

function is unknown. We also show that GLI1, which labels a subset of perivascular progenitors (29), is highly upregulated on postnatal CD90⁺CD146⁺ cells. Therefore, PDPN may represent a marker to enrich lung pericyte progenitors not fibroblasts. Recently, CD36 and CD97 were used to identify quiescent fibroblasts in human lung from patients with IPF (24). Future studies are needed to determine whether CD36 and CD97 are also expressed by perivascular-like cells identified in our study.

Despite these limitations, we noted a 5-fold reduction in the mesenchymal fraction with age, underscoring a significant remodeling process. Importantly, in congenial lung lesions and COPD, there was a re-emergence of the mesenchymal fraction. Recently, proliferation of NG2⁺ pericytes leading to excessive coverage of pulmonary capillaries and conversion to smooth muscle-like cells contributes, in part, to vascular remodeling found in human pulmonary arterial hypertension (48). MSCs, which derive from pericytes (10), are present in the tracheal aspirates of premature infants (11) and BALs of lung transplant recipients contributing to fibrotic obliteration of the small airways (12-14). Further, an increase recovery of mesenchymal cells in BALF is predictive of future BOS events after lung transplantation (3). The anatomical location and phenotype of the infiltrating mesenchymal cell lineage found within these fibrotic lesions was not reported (32, 56). Therefore, we hypothesize that the diminished regenerative capability of fully mature adult human lung may relate to an insufficient and/or impaired functioning mesenchymal compartment. Whether this entails CD90⁺PDGFR⁺CD146⁺ pericyte-like cells, which are highly enriched in both early postnatal, congenital lung lesions and COPD, remains to be determined. Therefore, future studies aimed at uncovering novel cellular and molecular targets within the mesenchymal compartment in chronic lung

725 disorders will rely on the availability and use of human lung tissue with refined 3D
726 models and advanced next generation sequencing technologies (47).

727

ACKNOWLEDGEMENTS

Tissues were provided by the Tissue Bank Bern. We thank Dr. Stefan Müller and Bernadette Nyfeler from the DBMR FACSLab Core facility, University of Bern for their assistance in performing the sorting experiments. We thank Andrea B. Stokes for assistance with the ELISA data. We also thank Ms. Blandina Esteves and Melanie Brügger, Institute of Virology and Immunology, University of Bern, for their assistance with the influenza infection.

AUTHOR CONTRIBUTIONS: conception & design – LW, PD, SRRH; Data acquisition – LW, PD, SZ, LF, SB, GJK, MPA, MB, BIOE, FB, CW, SS, AM, RWP, TMM, OTG, PKB, UM, RAS, SRRH; Data interpretation & analysis – LW, PD, SZ, SB, OTG, PKB, UM, SRRH; Drafting of Manuscript – LW, SRRH; Final Approval of manuscript – LW, RAS, SRRH; Accountability for all aspects of work – RAS, SRRH.

743 Table 1. Patient characteristics
744

Patient ID	Age (m)	Pathology	Notes	IF	H&E	FC/FACS
PL002	143	CPAM	Left lower lobe			Yes
PL003	10	Congenital lobar over inflation	Left upper lobe	EpCAM/CD73		Yes
*PL004	153	Chronic bronchiolitis/pneumonia	Left lower lobe	EpCAM/CD90/PDGFR α ,	Yes	Yes
PL005	5 days	Bronchial Atresia	Right middle lobe			Yes
PL006	11	CPAM	Upper right lobe	EpCAM/CD73		Yes
PL007	7	CPAM				Yes
*PL008	155	Chronic bronchiolitis/pneumonia	Right middle and lower lobe	EpCAM/CD90/PDGFR α , EpCAM/CD73	Yes	Yes
PL009	5	CPAM	Right lower lobe			Yes
PL010	9	Congenital lobar over inflation	Right middle lobe			Yes
PL012	1.5	Lobar emphysema	Left lobe	EpCAM/CD90/PDGFR α , EpCAM/CD73	Yes	Yes
PL013	4	CPAM, RSV infection	Right lower lobe	EpCAM/CD90/PDGFR α , EpCAM/CD73, EpCAM/CD90/SPC	Yes	Yes
PL014	54	CPAM with hybrid lesion, chronic infection	Left lower lobe	EpCAM/CD90/PDGFR α , EpCAM/CD73, EpCAM/CD90/SPC	Yes	Yes
PL015	73	Bronchogenic cyst	Right lower lobe			Yes
PL017	192	EBV-associated smooth-muscular tumor	Left lower lobe			Yes
PL018	181	Aspergilloma	Right lower lobe			Yes
PL019	6.5	CPAM	Right middle lobe	EpCAM/CD90/pro-SPC Ecad/CD90	Yes	Yes
PL020	6	CPAM	Right upper lobe			Yes
PL021	6	CPAM	Left Upper Lobe			Yes
PL022	7	CPAM	Right upper lobe			Yes

m, months; CPAM, congenital pulmonary airway malformation; RSV, respiratory syncytial virus
*same patient; FC, flow cytometry

Figure Legends

Figure 1. Flow cytometric analysis of human postnatal lung identifying

mesenchymal cell subsets. (A). Graphical overview of the strategy used to identify and

characterize mesenchymal cell subsets in human lung. (B) Representative bivariate flow

plots showing prominent mesenchymal fraction marked by EpCAM⁻CD45⁻CD31⁻CD14⁻ in

gate R4 (orange) in microscopically normal postnatal human lung. (C) Scatter plots

showing % of EpCAM⁻ compared with EpCAM⁺ fraction in postnatal lung. (D) Spearman

correlation showing mesenchymal fraction decrease with age. (E) Scatter plots

comparing EpCAM⁻ cells in postnatal with adult human lung. (F) Scatter plots showing %

EpCAM⁻ and EpCAM⁺ cells in adult human lung. (G) Representative bivariate plot of

mesenchymal EpCAM⁻ fraction (gate R4) after subgating for the mesenchymal markers

CD73 and CD90. (H) Scatter plots showing distribution of mesenchymal cell subsets.

Spearman correlation showing the change in CD90⁺CD73⁻ subset (I) and CD90⁺CD73⁺

subset (J) in postnatal human lung with age. (K) Representative H&E image of postnatal

lung section showing microscopically normal alveolar region. (L) Immunofluorescence

(IF) staining demonstrating that CD90⁺ (yellow arrowhead) and CD73⁺ cells (yellow

arrow) are expressed by a subset of cells in the alveolar region in close proximity to

epithelial progenitor cells marked by EpCAM (green, white arrowhead). Scale bar 50

µm. n = 19, biological replicates for postnatal lung; n = 15, biological replicates for adult

lung. Data are mean ± SD. Error bars show SD. Student t-test was used for comparison

of paired or unpaired parametric data. All tests were two-tailed. Analysis of means for

more than two groups by one-way ANOVA and multiple comparisons using post hoc

Newman-Keuls test. *p < 0.05 were considered significant.

Figure 2. CD90⁺ identifies heterogeneous population of mesenchymal cells in early postnatal human lung. (A-B) Schematic showing strategy for expansion of FACS-sorted mesenchymal cell subsets (A) and phase contrast images showing morphology in culture (B). Scale bar 50 μ m (C) Representative images of Oil Red O stain after 21 days of adipogenic differentiation. mRNA expression levels of key genes involved in adipogenesis are shown below. Scale bar 50 μ m (D) Representative image of Alizarin Red S stain after 21 days in osteogenic induction media. mRNA expression levels of key genes involved in osteogenesis are shown below. Relative expression to adult BM-MSCs. n = 3-4, biological replicates. Scale bar 2000 μ m (E-F) Representative image of micromass pellet cultures generated from adipose or bone marrow-derived MSCs (E) and postnatal lung-derived CD90⁺ subsets (F) after 21 days in chondrogenic induction media stained with Toluidine blue. Scale bar 200 μ m. Data are mean \pm SD. Error bars show SD. Analysis of means for more than two groups by one-way ANOVA and multiple comparisons using post hoc Newman-Keuls test. *p<0.05 were considered significant.

Figure 3. CD90⁺ mesenchymal cells support formation of lung organoids with immature cystic-like epithelium and expand in congenital lung lesions. (A) Schematic illustration showing experimental setup to generate alveolar organoids. (B) Representative immunofluorescence image of alveolar organoids reveals epithelial saccule-like structures positive for E-cadherin (green) surrounded by PDGFR α ⁺ mesenchymal cells (3D surface, top, xy plane). Magnified boxed region (a) of a Z stack from an individual organoid shows saccule-like features, multicellular organization and lumen formation. Scale bars: 100 μ m and 30 μ m. (C) IF staining of the unaffected

postnatal human lung showing a subset of CD90 cells that also co-express PDGFR α (yellow arrow) in close proximity to EpCAM⁺ cells (white arrowhead). Inset panel shows an enlarged view of the highlighted area (white rectangle) showing a cluster of CD90⁺ cells (red) and EpCAM⁺ cells (green). Scale bar 50 μ m. (D) Relative mRNA levels in organoids from 3D coculture with autologous CD90⁺ mesenchymal cells compared to 2D culture conditions and postnatal lung tissue. mRNA level in postnatal lung tissue is set at one. n = 3-4, biological replicates. (E, H, K) Histological analysis of CPAM with chronic infection (E), CPAM with RSV infection (H) and chronic bronchiolitis (K). IF staining of lung sections showing EpCAM (green), CD90 (red) and PDGFR α (white) cells in CPAM with chronic infection (F-G), CPAM with RSV infection (I-J) chronic bronchiolitis (L-M). Boxed areas are magnified in right panels (F, I, L) and channels are separated without DAPI to highlight co-stained regions. Thickened interstitial spaces and dysplastic alveolar epithelium filled with CD90⁺ (yellow arrow) and CD90⁺PDGFR α ⁺ cells (yellow arrowhead). Alv, alveolar region. Scale bar 200 μ m (E, F, H), 100 μ m (I, K, L), 50 μ m (G, J, M). Values are presented as mean \pm SD. Error bars show SD. Analysis by one-way ANOVA and multiple comparisons using post hoc Newman-Keuls. *p<0.05. ND, not detected.

Figure 4. Presence of CD90⁺CD146⁺ mesenchymal cell subset that can be targeted by virosomes and live influenza A virus. (A) Representative bivariate plots showing expression of pericyte markers CD146 and NOTCH3 in CD90⁺CD73⁻ and CD90⁺CD73⁺ cells in postnatal human lung. (B) Scatter plots showing expression of CD146, as a % of total counted events (n = 6, biological replicates). (C) Representative flow cytometric density plots showing expression for common mesenchymal markers found to be

expressed on pericytes and fibroblasts in prospectively isolated CD90⁺CD73⁻ lacking CD146 (red, top panels) and a subset expressing CD146 (blue, bottom panels) (n = 3 - 5, biological replicates). (D) CD90⁺CD146⁺ mesenchymal cells exposed to virosomes or liposomes for 24h. Representative histogram plots show uptake of virosomes or liposomes by measuring Atto647 fluorescence signal by flow cytometry. (E) Scatter plots showing the change in Atto647 fluorescent signal (gMFI). (F) Representative FACS plots showing infection of postnatal CD90⁺CD146⁺ mesenchymal cells with live H1N1 influenza virus (PR8 strain) after 24h compared to mock infection. (G) Representative FACS plots showing baseline fluorescence in unstained CD90⁺CD146⁺ mesenchymal cells (left plot) or isotype control for influenza nuclear protein. (H) Scatter plots showing % of CD90⁺CD146⁺ mesenchymal cells infected with live H1N1 over 48 hours. n = 3, biological replicates. (I) Scatter plots showing infectious titer of live virus shed in the culture supernatants. n = 3, biological replicates. Data are presented as mean ± SD. Error bars show SD. Student t-test was used for comparison of paired data. All tests were two-tailed. *p<0.05 were considered significant.

Figure 5. Characterization of CD90⁺CD146⁺ mesenchymal cells from chronic obstructive pulmonary disease (COPD) patients. (A) Representative bivariate FACS plot showing a prominent EpCAM⁻ mesenchymal fraction (gate R4, orange) subgated from single, live cells from a COPD patient. (B-C) Scatter plots showing percentage of EpCAM⁻ cells (B), and EpCAM⁻/EpCAM⁺ ratio (C) in COPD (n = 15, biological replicates) (●) and non-COPD (n = 15, biological replicates) (■) lung tissue. (D) Scatter plots showing distribution of mesenchymal cell subsets. (E) Scatter plots showing CD146 is expressed in CD90⁺CD73⁻ and CD90⁺CD73⁻ mesenchymal cells in non-COPD

compared with COPD tissue (n = 6, non-COPD and n = 11, COPD). (F) Phase contrast image showing morphology of CD90⁺CD146⁺ mesenchymal cells from COPD compared with postnatal lung. Scale bar 50 μ m. (G) mRNA expression of selected genes of various mesenchymal markers and functional categories specific to the lung in CD90⁺CD146⁺ mesenchymal cells from microscopically normal postnatal human lung (n = 4, biological replicates) and COPD patients (n = 4, biological replicates). Human lung fibroblast was set at one (not shown). (H) mRNA expression of selected genes in CD90⁺CD146⁺ mesenchymal cells from COPD (n =4) compared with postnatal human lung (n = 4, biological replicates) treated with TGF β 1 (5ng/ml) over 72 hours with or without metformin (0.5mM). Human lung fibroblasts was set at one. Values are presented as mean \pm SD. Error bars show SD. Analysis by one-way ANOVA and multiple comparisons using post hoc Newman-Keuls. *p<0.05. ND, not detected.

Figure 6. CD90⁺CD146⁺ cells from COPD patients fail to support microvessel formation. (A) Microfluidic chip of *in vitro* perfusable microvasculature network. (B) Schematic overview of chip seeding process. Microvessel characterization on day 7 for postnatal (C) and adult COPD (D) CD90⁺CD146⁺ cells stained with CD31 (red) and shown as a circular image of central chamber. Scale bar 250 μ m (E, F) Series of rectangular images from a part of the central chamber stained for different marker for postnatal (E) and adult COPD (F). Scale bar 100 μ m. Orthogonal view of the overlay of the images showing open lumens (white asterisk) in postnatal (G) and adult COPD (H). Scale bar 100 μ m. (I) Representative images showing addition of 70 kDa RITC-dextran and perfusion of 3D microvasculature network (white arrows) formed with postnatal CD90⁺CD146⁺ cells (left panels) and lack of perfusion in COPD (right panels). Images

868 represent a segment of the central chamber and are overlays of the red channel and
869 bright field at specific time points. Scale bar 200 μm . (J, K) IF staining shows CD31⁺
870 (red) microvessel-like structure after 7 days in the presence of antifibrinolytic agent ϵ -
871 Aminocaproic acid (EACA, 200 $\mu\text{g}/\text{ml}$) for postnatal (J) and COPD (K) CD90⁺CD146⁺
872 cells cultured with HUVECs. Scale bar 250 μm . (L, M) Schematic highlighting 3D
873 microvasculature structure in the central chamber with orthogonal view of the overlay
874 from serial images showing open lumens in postnatal (L) and in COPD (M). Scale bar
875 100 μm . (N) Representative image showing RITC-dextran perfusion of 3D
876 microvasculature network in the presence of EACA for postnatal left panels) and COPD
877 (right panels) microvasculature structures. Scale bar 200 μm . (O) Bar graph showing
878 quantification of vessel diameter. $n = 4$, biological replicates. Data presented as mean \pm
879 SD. Student t-test was used for comparison of unpaired parametric data. All tests were
880 two-tailed. * $p < 0.05$ were considered significant.

881

REFERENCES

1. **Ahlbrecht K, and McGowan SE.** In search of the elusive lipofibroblast in human lungs. *American journal of physiology Lung cellular and molecular physiology* 307: L605-608, 2014.
2. **Astarita JL, Acton SE, and Turley SJ.** Podoplanin: emerging functions in development, the immune system, and cancer. *Frontiers in immunology* 3: 283, 2012.
3. **Badri L, Murray S, Liu LX, Walker NM, Flint A, Wadhwa A, Chan KM, Toews GB, Pinsky DJ, Martinez FJ, and Lama VN.** Mesenchymal stromal cells in bronchoalveolar lavage as predictors of bronchiolitis obliterans syndrome. *American journal of respiratory and critical care medicine* 183: 1062-1070, 2011.
4. **Barkauskas CE, Counce MJ, Rackley CR, Bowie EJ, Keene DR, Stripp BR, Randell SH, Noble PW, and Hogan BL.** Type 2 alveolar cells are stem cells in adult lung. *The Journal of clinical investigation* 123: 3025-3036, 2013.
5. **Barnes PJ.** Targeting cytokines to treat asthma and chronic obstructive pulmonary disease. *Nature reviews Immunology* 2018.
6. **Barron L, Gharib SA, and Duffield JS.** Lung Pericytes and Resident Fibroblasts: Busy Multitaskers. *The American journal of pathology* 186: 2519-2531, 2016.
7. **Beers MF, and Morrissey EE.** The three R's of lung health and disease: repair, remodeling, and regeneration. *The Journal of clinical investigation* 121: 2065-2073, 2011.
8. **Bichsel CA, Wang L, Froment L, Berezowska S, Muller S, Dorn P, Marti TM, Peng RW, Geiser T, Schmid RA, Guenat OT, and Hall SRR.** Increased PD-L1 expression and IL-6 secretion characterize human lung tumor-derived perivascular-like cells that promote vascular leakage in a perfusable microvasculature model. *Scientific reports* 7: 10636, 2017.
9. **Blom RA, Erni ST, Krempaska K, Schaerer O, van Dijk RM, Amacker M, Moser C, Hall SR, von Garnier C, and Blank F.** A Triple Co-Culture Model of the Human Respiratory Tract to Study Immune-Modulatory Effects of Liposomes and Virosomes. *PloS one* 11: e0163539, 2016.
10. **Bozyk PD, Popova AP, Bentley JK, Goldsmith AM, Linn MJ, Weiss DJ, and Hershenson MB.** Mesenchymal stromal cells from neonatal tracheal aspirates demonstrate a pattern of lung-specific gene expression. *Stem cells and development* 20: 1995-2007, 2011.
11. **Collins JJP, Lithopoulos MA, Dos Santos CC, Issa N, Mobius MA, Ito C, Zhong S, Vadivel A, and Thebaud B.** Impaired Angiogenic Supportive Capacity and Altered Gene Expression Profile of Resident CD146(+) Mesenchymal Stromal Cells Isolated from Hyperoxia-Injured Neonatal Rat Lungs. *Stem cells and development* 27: 1109-1124, 2018.
12. **Crisan M, Yap S, Casteilla L, Chen CW, Corselli M, Park TS, Andriolo G, Sun B, Zheng B, Zhang L, Norotte C, Teng PN, Traas J, Schugar R, Deasy BM, Badylak S, Buhring HJ, Giacobino JP, Lazzari L, Huard J, and Peault B.** A perivascular origin for mesenchymal stem cells in multiple human organs. *Cell Stem Cell* 3: 301-313, 2008.
13. **Crystal RG.** Airway basal cells. The "smoking gun" of chronic obstructive pulmonary disease. *American journal of respiratory and critical care medicine* 190: 1355-1362, 2014.
14. **Duong H, Wu B, and Tawil B.** Modulation of 3D fibrin matrix stiffness by intrinsic fibrinogen-thrombin compositions and by extrinsic cellular activity. *Tissue engineering Part A* 15: 1865-1876, 2009.
15. **Durell J, Thakkar H, Gould S, Fowler D, and Lakhoo K.** Pathology of asymptomatic, prenatally diagnosed cystic lung malformations. *J Pediatr Surg* 51: 231-235, 2016.
16. **El Agha E, Herold S, Al Alam D, Quantius J, MacKenzie B, Carraro G, Moiseenko A, Chao CM, Minoo P, Seeger W, and Bellusci S.** Fgf10-positive cells represent a progenitor cell population during lung development and postnatally. *Development* 141: 296-306, 2014.
17. **El Agha E, Moiseenko A, Kheirollahi V, De Langhe S, Crnkovic S, Kwapiszewska G, Szibor M, Kosanovic D, Schwind F, Schermuly RT, Henneke I, MacKenzie B, Quantius J, Herold S, Ntokou A, Ahlbrecht K, Braun T, Morty RE, Gunther A, Seeger W, and Bellusci S.** Two-Way Conversion between

- Lipogenic and Myogenic Fibroblastic Phenotypes Marks the Progression and Resolution of Lung Fibrosis. *Cell Stem Cell* 20: 571, 2017.
18. **Engler AJ, Sen S, Sweeney HL, and Discher DE.** Matrix elasticity directs stem cell lineage specification. *Cell* 126: 677-689, 2006.
 19. **Geiger S, Hirsch D, and Hermann FG.** Cell therapy for lung disease. *European respiratory review : an official journal of the European Respiratory Society* 26: 2017.
 20. **Ghosh M, Miller YE, Nakachi I, Kwon JB, Baron AE, Brantley AE, Merrick DT, Franklin WA, Keith RL, and Vandivier RW.** Exhaustion of Airway Basal Progenitor Cells in Early and Established Chronic Obstructive Pulmonary Disease. *American journal of respiratory and critical care medicine* 197: 885-896, 2018.
 21. **Glassberg MK, Minkiewicz J, Toonkel RL, Simonet ES, Rubio GA, DiFede D, Shafazand S, Khan A, Pujol MV, LaRussa VF, Lancaster LH, Rosen GD, Fishman J, Mageto YN, Mendizabal A, and Hare JM.** Allogeneic Human Mesenchymal Stem Cells in Patients With Idiopathic Pulmonary Fibrosis via Intravenous Delivery (AETHER): A Phase I Safety Clinical Trial. *Chest* 151: 971-981, 2017.
 22. **Greenbaum A, Hsu YM, Day RB, Schuettpeitz LG, Christopher MJ, Borgerding JN, Nagasawa T, and Link DC.** CXCL12 in early mesenchymal progenitors is required for haematopoietic stem-cell maintenance. *Nature* 495: 227-230, 2013.
 23. **Hall SR, Jiang Y, Leary E, Yavanian G, Eminli S, O'Neill DW, and Marasco WA.** Identification and isolation of small CD44-negative mesenchymal stem/progenitor cells from human bone marrow using elutriation and polychromatic flow cytometry. *Stem Cells Transl Med* 2: 567-578, 2013.
 24. **Heinzelmann K, Lehmann M, Gerckens M, Noskovicova N, Frankenberger M, Lindner M, Hatz R, Behr J, Hilgendorff A, Konigshoff M, and Eickelberg O.** Cell-surface phenotyping identifies CD36 and CD97 as novel markers of fibroblast quiescence in lung fibrosis. *American journal of physiology Lung cellular and molecular physiology* 315: L682-L696, 2018.
 25. **Herzenberg LA, Tung J, Moore WA, Herzenberg LA, and Parks DR.** Interpreting flow cytometry data: a guide for the perplexed. *Nature immunology* 7: 681-685, 2006.
 26. **Hung CF, Mittelsteadt KL, Brauer R, McKinney BL, Hallstrand TS, Parks WC, Chen P, Schnapp LM, Liles WC, Duffield JS, and Altemeier WA.** Lung pericyte-like cells are functional interstitial immune sentinel cells. *American journal of physiology Lung cellular and molecular physiology* 312: L556-L567, 2017.
 27. **Kheirollahi V, Wasnick RM, Biasin V, Vazquez-Armendariz AI, Chu X, Moiseenko A, Weiss A, Wilhelm J, Zhang JS, Kwapiszewska G, Herold S, Schermuly RT, Mari B, Li X, Seeger W, Gunther A, Bellusci S, and El Agha E.** Metformin induces lipogenic differentiation in myofibroblasts to reverse lung fibrosis. *Nature communications* 10: 2987, 2019.
 28. **Kotton DN, and Morrissey EE.** Lung regeneration: mechanisms, applications and emerging stem cell populations. *Nature medicine* 20: 822-832, 2014.
 29. **Kramann R, Schneider RK, DiRocco DP, Machado F, Fleig S, Bondzie PA, Henderson JM, Ebert BL, and Humphreys BD.** Perivascular Gli1+ progenitors are key contributors to injury-induced organ fibrosis. *Cell Stem Cell* 16: 51-66, 2015.
 30. **Kranenburg AR, de Boer WI, Alagappan VK, Sterk PJ, and Sharma HS.** Enhanced bronchial expression of vascular endothelial growth factor and receptors (Flk-1 and Flt-1) in patients with chronic obstructive pulmonary disease. *Thorax* 60: 106-113, 2005.
 31. **Kratzer A, Chu HW, Salys J, Moumen Z, Leberl M, Bowler R, Cool C, Zamora M, and Taraseviciene-Stewart L.** Endothelial cell adhesion molecule CD146: implications for its role in the pathogenesis of COPD. *The Journal of pathology* 230: 388-398, 2013.
 32. **Lama VN, Smith L, Badri L, Flint A, Andrei AC, Murray S, Wang Z, Liao H, Toews GB, Krebsbach PH, Peters-Golden M, Pinsky DJ, Martinez FJ, and Thannickal VJ.** Evidence for tissue-resident mesenchymal stem cells in human adult lung from studies of transplanted allografts. *The Journal of clinical investigation* 117: 989-996, 2007.

33. **Lemos DR, and Duffield JS.** Tissue-resident mesenchymal stromal cells: Implications for tissue-specific antifibrotic therapies. *Science translational medicine* 10: 2018.
34. **Lignelli E, Palumbo F, Myti D, and Morty RE.** Recent advances in our understanding of the mechanisms of lung alveolarization and bronchopulmonary dysplasia. *American journal of physiology Lung cellular and molecular physiology* 317: L832-L887, 2019.
35. **Maclay JD, McAllister DA, Mills NL, Paterson FP, Ludlam CA, Drost EM, Newby DE, and Macnee W.** Vascular dysfunction in chronic obstructive pulmonary disease. *American journal of respiratory and critical care medicine* 180: 513-520, 2009.
36. **Mendes ES, Campos MA, and Wanner A.** Airway blood flow reactivity in healthy smokers and in ex-smokers with or without COPD. *Chest* 129: 893-898, 2006.
37. **Mercer PF, Woodcock HV, Eley JD, Plate M, Sulikowski MG, Durrenberger PF, Franklin L, Nanthakumar CB, Man Y, Genovese F, McAnulty RJ, Yang S, Maher TM, Nicholson AG, Blanchard AD, Marshall RP, Lukey PT, and Chambers RC.** Exploration of a potent PI3 kinase/mTOR inhibitor as a novel anti-fibrotic agent in IPF. *Thorax* 71: 701-711, 2016.
38. **Mobius MA, Freund D, Vadivel A, Koss S, McConaghy S, Ohls RK, Rudiger M, and Thebaud B.** Oxygen Disrupts Human Fetal Lung Mesenchymal Cells. Implications for Bronchopulmonary Dysplasia. *American journal of respiratory cell and molecular biology* 60: 592-600, 2019.
39. **Nabhan AN, Brownfield DG, Harbury PB, Krasnow MA, and Desai TJ.** Single-cell Wnt signaling niches maintain stemness of alveolar type 2 cells. *Science* 359: 1118-1123, 2018.
40. **Park J, Ivey MJ, Deana Y, Riggsbee KL, Sorensen E, Schwabl V, Sjoberg C, Hjertberg T, Park GY, Swonger JM, Rosengreen T, Morty RE, Ahlbrecht K, and Tallquist MD.** The Tcf21 lineage constitutes the lung lipofibroblast population. *American journal of physiology Lung cellular and molecular physiology* 316: L872-L885, 2019.
41. **Parks DR, Roederer M, and Moore WA.** A new "Logicle" display method avoids deceptive effects of logarithmic scaling for low signals and compensated data. *Cytometry A* 69: 541-551, 2006.
42. **Pogoriler J, Swarr D, Kreiger P, Adzick NS, and Peranteau W.** Congenital Cystic Lung Lesions: Redefining the Natural Distribution of Subtypes and Assessing the Risk of Malignancy. *The American journal of surgical pathology* 43: 47-55, 2019.
43. **Popova AP, Bentley JK, Cui TX, Richardson MN, Linn MJ, Lei J, Chen Q, Goldsmith AM, Pryhuber GS, and Hershenson MB.** Reduced platelet-derived growth factor receptor expression is a primary feature of human bronchopulmonary dysplasia. *American journal of physiology Lung cellular and molecular physiology* 307: L231-239, 2014.
44. **Popova AP, Bozyk PD, Bentley JK, Linn MJ, Goldsmith AM, Schumacher RE, Weiner GM, Filbrun AG, and Hershenson MB.** Isolation of tracheal aspirate mesenchymal stromal cells predicts bronchopulmonary dysplasia. *Pediatrics* 126: e1127-1133, 2010.
45. **Rafii S, Cao Z, Lis R, Siempos, II, Chavez D, Shido K, Rabbany SY, and Ding BS.** Platelet-derived SDF-1 primes the pulmonary capillary vascular niche to drive lung alveolar regeneration. *Nat Cell Biol* 17: 123-136, 2015.
46. **Reicherzer T, Haffner S, Shahzad T, Gronbach J, Mysliwietz J, Hubener C, Hasbargen U, Gertheiss J, Schulze A, Bellusci S, Morty RE, Hilgendorff A, and Ehrhardt H.** Activation of the NF-kappaB pathway alters the phenotype of MSCs in the tracheal aspirates of preterm infants with severe BPD. *American journal of physiology Lung cellular and molecular physiology* 315: L87-L101, 2018.
47. **Reyfman PA, Walter JM, Joshi N, Anekalla KR, McQuattie-Pimentel AC, Chiu S, Fernandez R, Akbarpour M, Chen CI, Ren Z, Verma R, Abdala-Valencia H, Nam K, Chi M, Han S, Gonzalez-Gonzalez FJ, Soberanes S, Watanabe S, Williams KJN, Flozak AS, Nicholson TT, Morgan VK, Winter DR, Hinchcliff M, Hrusch CL, Guzy RD, Bonham CA, Sperling AI, Bag R, Hamanaka RB, Mutlu GM, Yeldandi AV, Marshall SA, Shilatifard A, Amaral LAN, Perlman H, Sznajder JI, Argento AC, Gillespie CT, Dematte J, Jain M, Singer BD, Ridge KM, Lam AP, Bharat A, Bhorade SM, Gottardi CJ, Budinger GRS, and Misharin AV.**

Single-Cell Transcriptomic Analysis of Human Lung Provides Insights into the Pathobiology of Pulmonary Fibrosis. *American journal of respiratory and critical care medicine* 2018.

48. **Ricard N, Tu L, Le Hires M, Huertas A, Phan C, Thuillet R, Sattler C, Fadel E, Seferian A, Montani D, Dorfmueller P, Humbert M, and Guignabert C.** Increased pericyte coverage mediated by endothelial-derived fibroblast growth factor-2 and interleukin-6 is a source of smooth muscle-like cells in pulmonary hypertension. *Circulation* 129: 1586-1597, 2014.

49. **Smith LR, Cho S, and Discher DE.** Stem Cell Differentiation is Regulated by Extracellular Matrix Mechanics. *Physiology* 33: 16-25, 2018.

50. **Staudt MR, Buro-Auriemma LJ, Walters MS, Salit J, Vincent T, Shaykhiev R, Mezey JG, Tilley AE, Kaner RJ, Ho MW, and Crystal RG.** Airway Basal stem/progenitor cells have diminished capacity to regenerate airway epithelium in chronic obstructive pulmonary disease. *American journal of respiratory and critical care medicine* 190: 955-958, 2014.

51. **Swarr DT, Peranteau WH, Pogoriler J, Frank DB, Adzick NS, Hedrick HL, Morley M, Zhou S, and Morrissey EE.** Novel Molecular and Phenotypic Insights into Congenital Lung Malformations. *American journal of respiratory and critical care medicine* 2018.

52. **Tahedi D, Wirkes A, Tschanz SA, Ochs M, and Muhlfeld C.** How common is the lipid body-containing interstitial cell in the mammalian lung? *American journal of physiology Lung cellular and molecular physiology* 307: L386-394, 2014.

53. **Tamura S, Suzuki-Inoue K, Tsukiji N, Shirai T, Sasaki T, Osada M, Satoh K, and Ozaki Y.** Podoplanin-positive periarteriolar stromal cells promote megakaryocyte growth and proplatelet formation in mice by CLEC-2. *Blood* 127: 1701-1710, 2016.

54. **Tata PR, and Rajagopal J.** Plasticity in the lung: making and breaking cell identity. *Development* 144: 755-766, 2017.

55. **Togo S, Holz O, Liu X, Sugiura H, Kamio K, Wang X, Kawasaki S, Ahn Y, Fredriksson K, Skold CM, Mueller KC, Branscheid D, Welker L, Watz H, Magnussen H, and Rennard SI.** Lung fibroblast repair functions in patients with chronic obstructive pulmonary disease are altered by multiple mechanisms. *American journal of respiratory and critical care medicine* 178: 248-260, 2008.

56. **Walker N, Badri L, Wettlaufer S, Flint A, Sajjan U, Krebsbach PH, Keshamouni VG, Peters-Golden M, and Lama VN.** Resident tissue-specific mesenchymal progenitor cells contribute to fibrogenesis in human lung allografts. *The American journal of pathology* 178: 2461-2469, 2011.

57. **Weibel ER.** On pericytes, particularly their existence on lung capillaries. *Microvascular research* 8: 218-235, 1974.

58. **Wilson CL, Stephenson SE, Higuero JP, Feghali-Bostwick C, Hung CF, and Schnapp LM.** Characterization of human PDGFR-beta-positive pericytes from IPF and non-IPF lungs. *American journal of physiology Lung cellular and molecular physiology* 315: L991-L1002, 2018.

59. **Xi Y, Kim T, Brumwell AN, Driver IH, Wei Y, Tan V, Jackson JR, Xu J, Lee DK, Gotts JE, Matthay MA, Shannon JM, Chapman HA, and Vaughan AE.** Local lung hypoxia determines epithelial fate decisions during alveolar regeneration. *Nat Cell Biol* 19: 904-914, 2017.

60. **Xie T, Wang Y, Deng N, Huang G, Taghavifar F, Geng Y, Liu N, Kulur V, Yao C, Chen P, Liu Z, Stripp B, Tang J, Liang J, Noble PW, and Jiang D.** Single-Cell Deconvolution of Fibroblast Heterogeneity in Mouse Pulmonary Fibrosis. *Cell reports* 22: 3625-3640, 2018.

61. **Zeinali S, Bichsel CA, Hobi N, Funke M, Marti TM, Schmid RA, Guenat OT, and Geiser T.** Human microvasculature-on-a chip: anti-neovascrogenic effect of nintedanib in vitro. *Angiogenesis* 21: 861-871, 2018.

62. **Zepp JA, Zacharias WJ, Frank DB, Cavanaugh CA, Zhou S, Morley MP, and Morrissey EE.** Distinct Mesenchymal Lineages and Niches Promote Epithelial Self-Renewal and Myofibrogenesis in the Lung. *Cell* 170: 1134-1148 e1110, 2017.

Figure 1

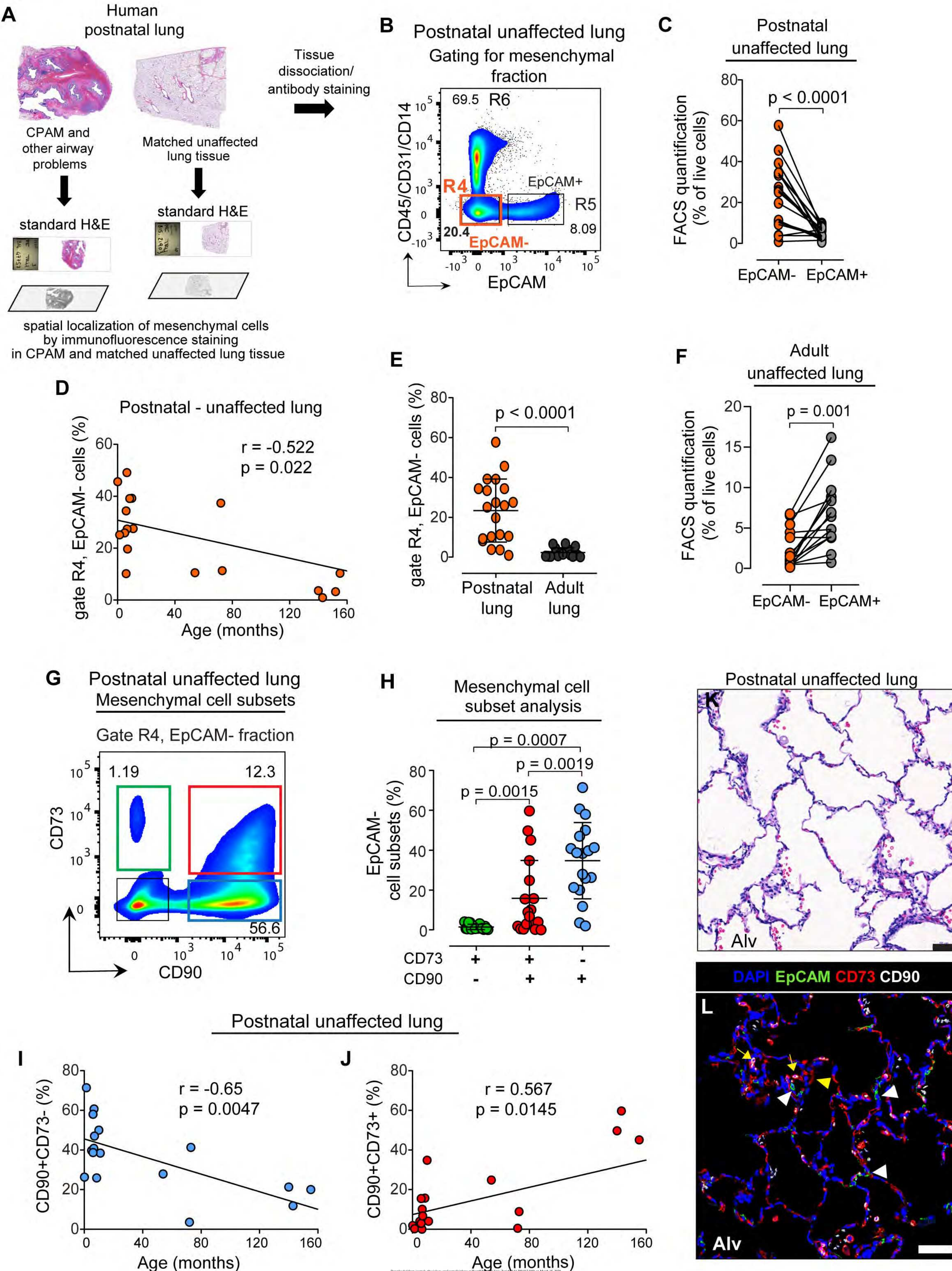
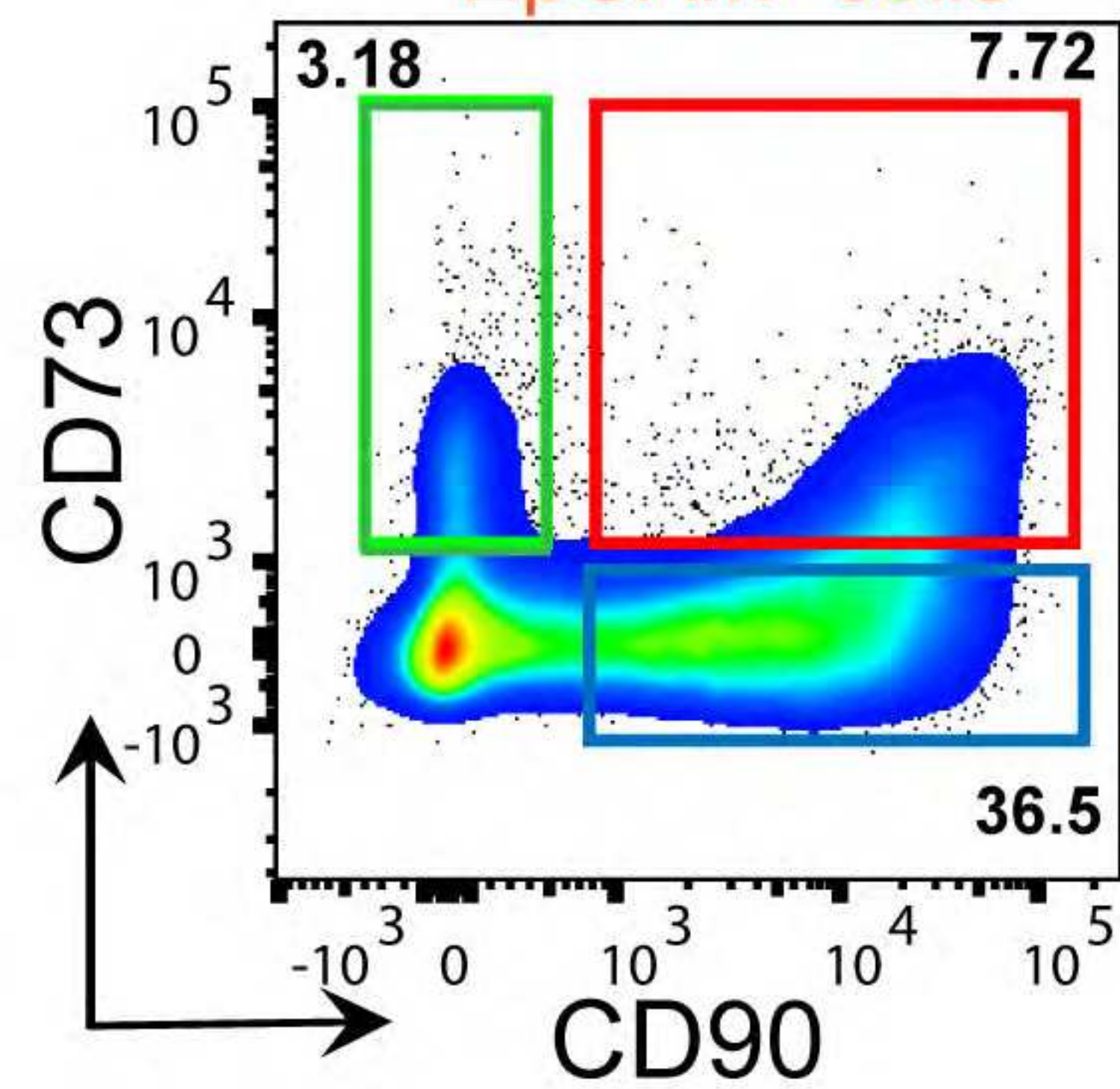


Figure 2**A**

PL020 - posnatal unaffected lung
Gated from single, live

EpCAM⁻ cells



FACS sort
mesenchymal cells

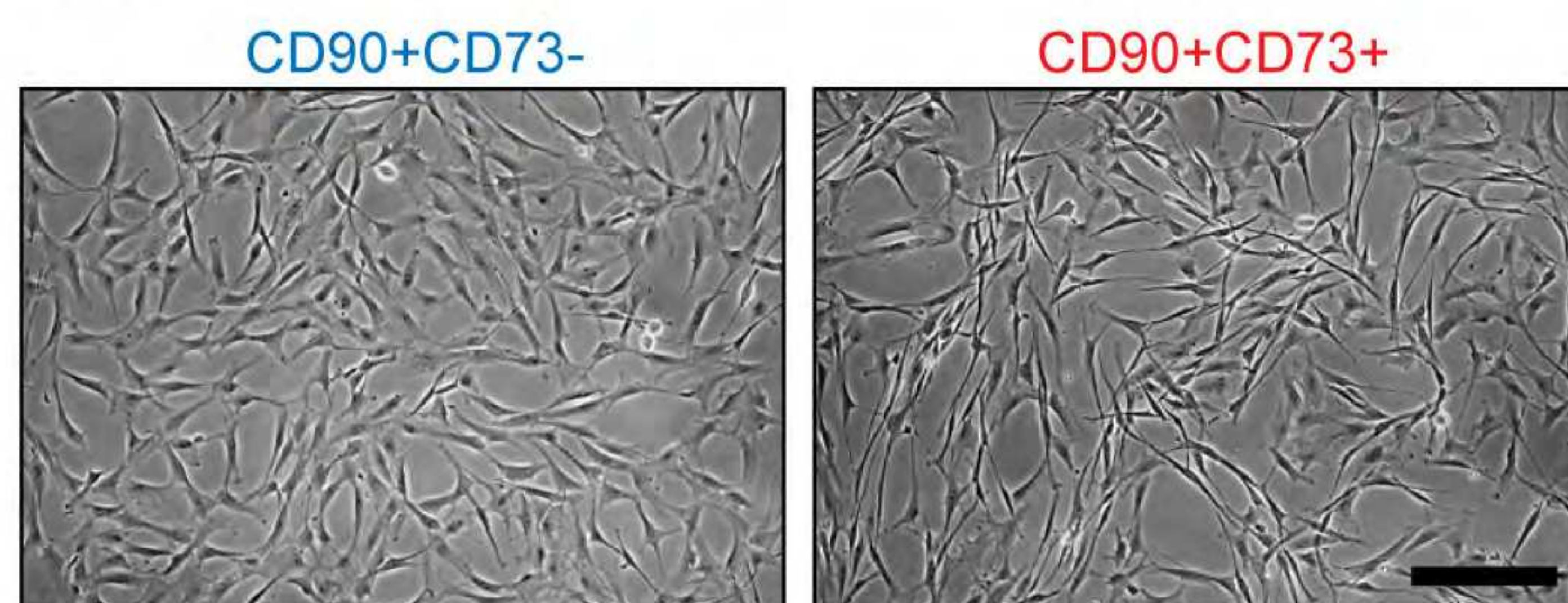
CD90+CD73⁻ CD90+CD73⁺

B

Seed
↓
D0

Mesenchymal media
EGF, FGF2, human insulin, 1%FBS

Expansion, analysis and characterization
↓
D12-14

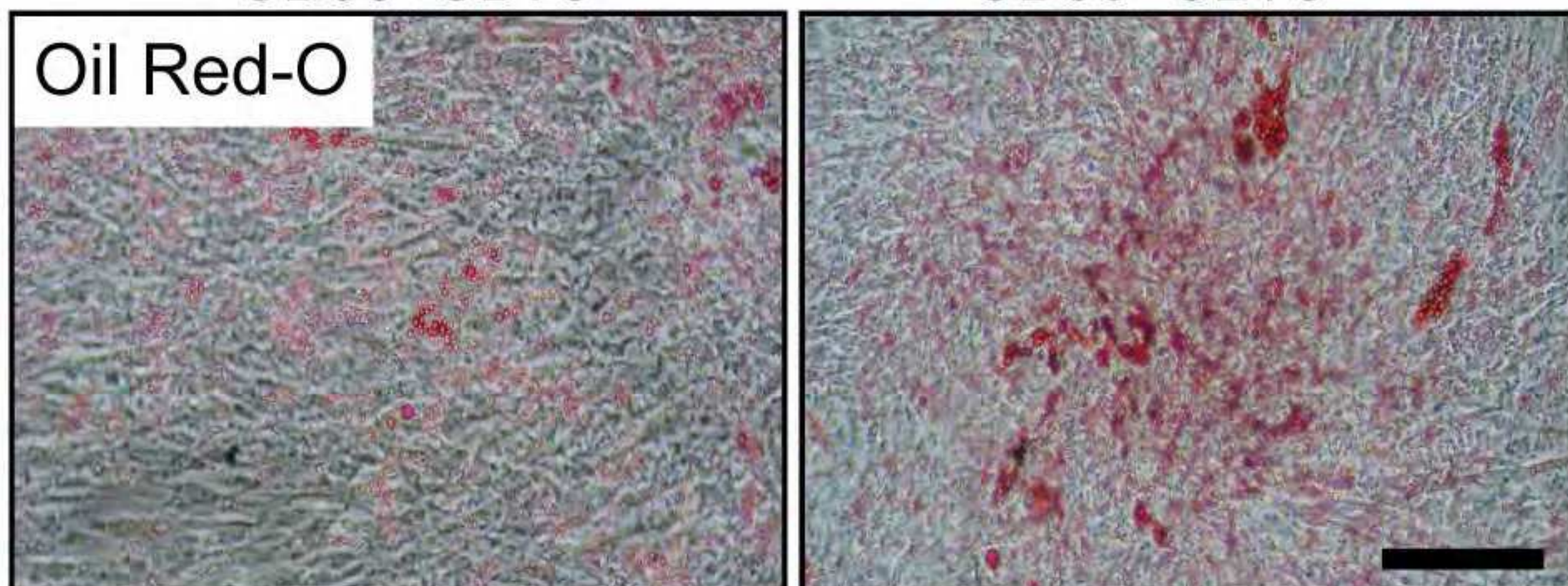


Mesenchymal differentiation

C

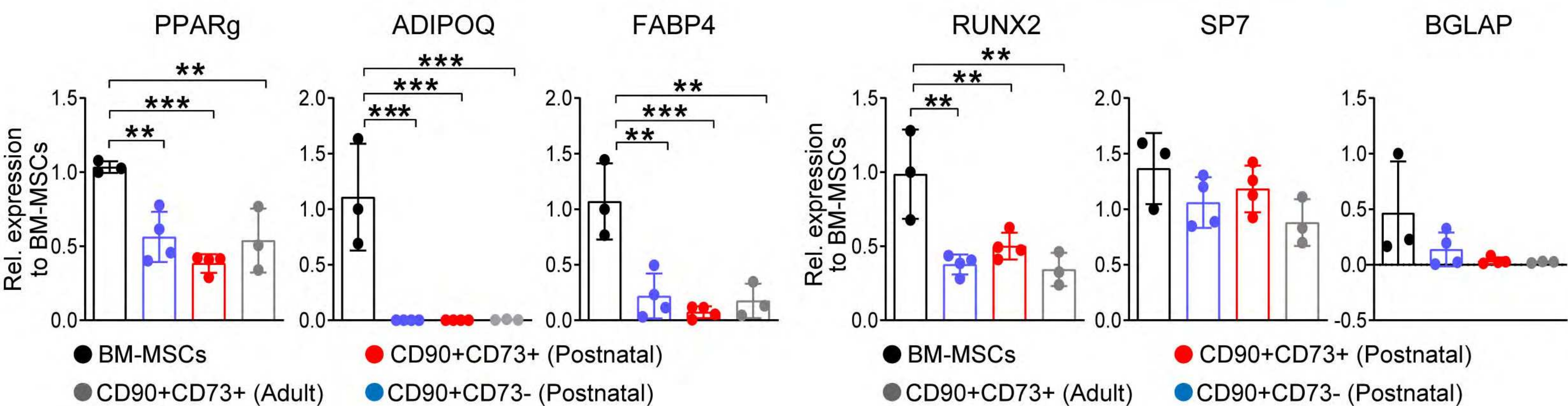
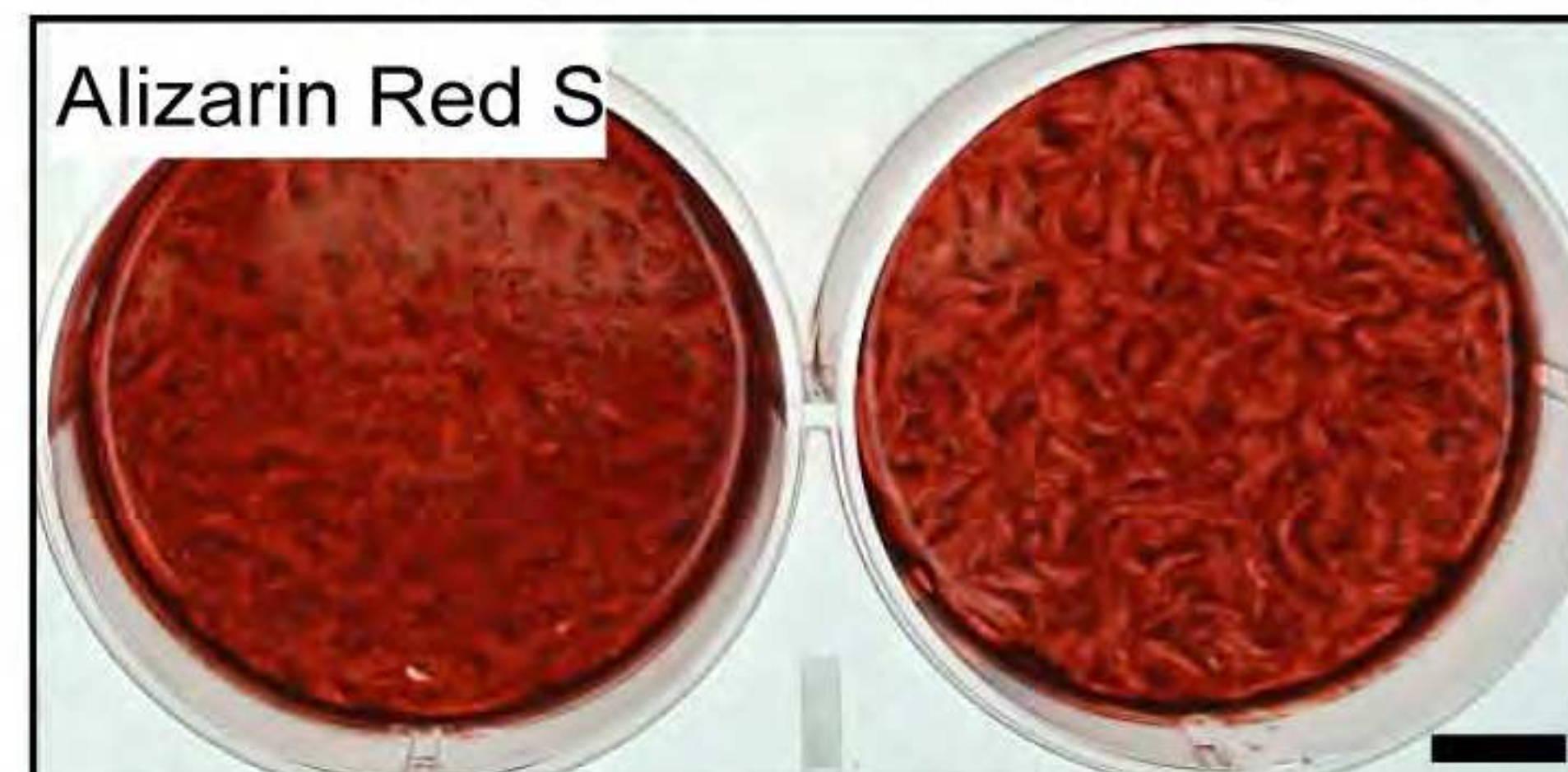
CD90+CD73⁻

CD90+CD73⁺

**D**

CD90+CD73⁻

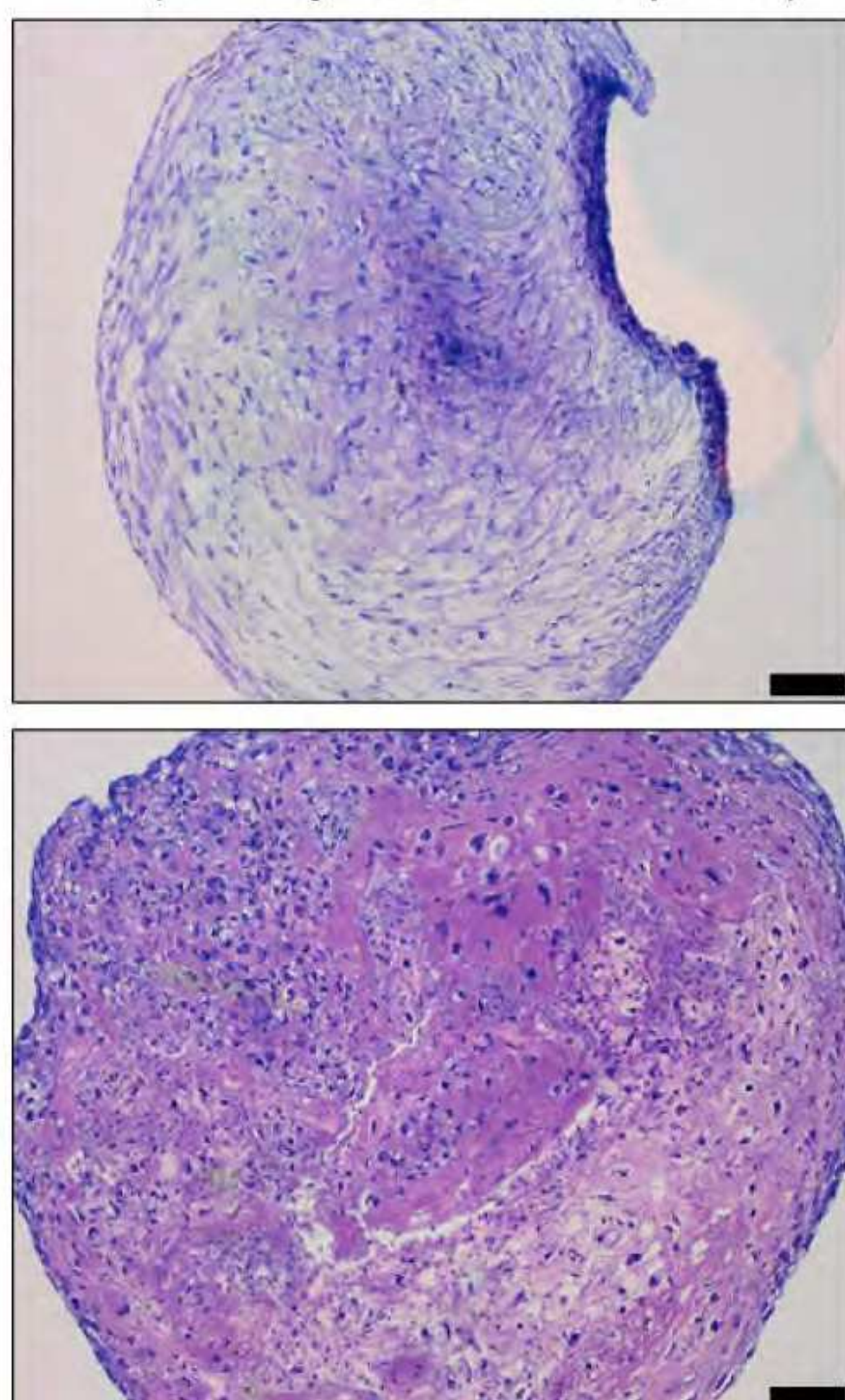
CD90+CD73⁺

**E**

Toluidine blue
(21 day micromass pellet)

A-MSCs

BM-MSCs

**F**

Donor 1

Donor 2

CD90+CD73⁻

CD90+CD73⁺

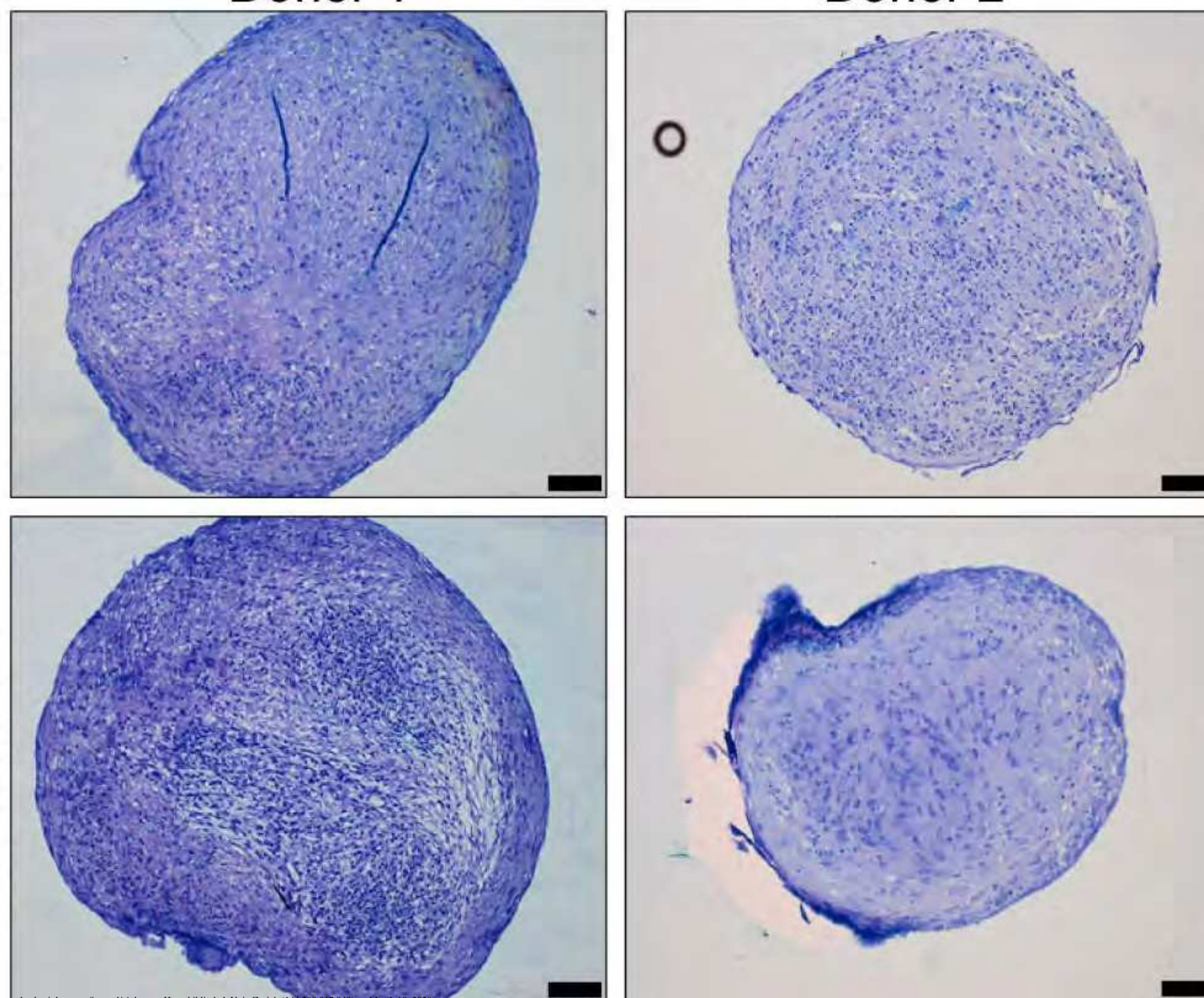


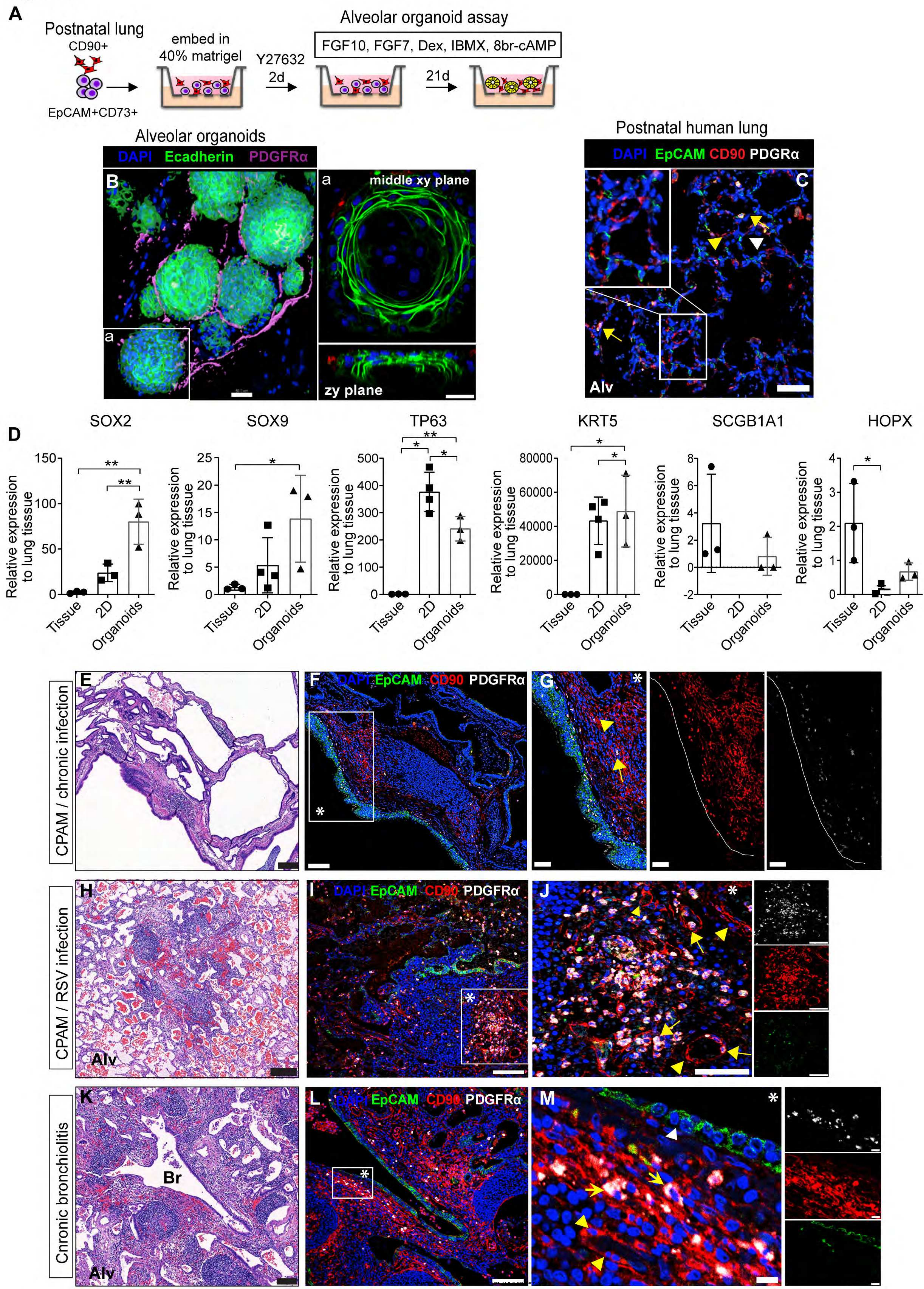
Figure 3

Figure 4

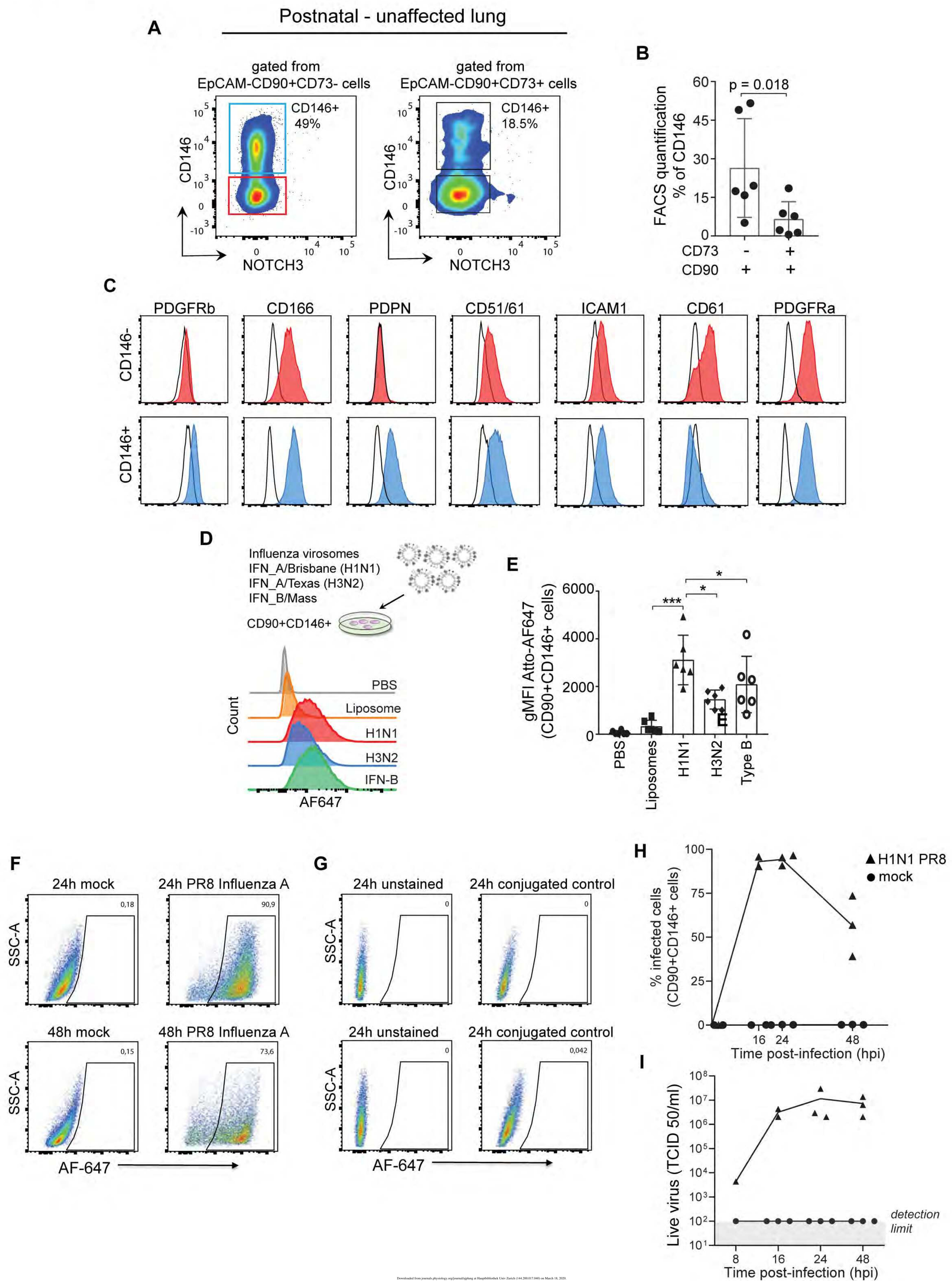


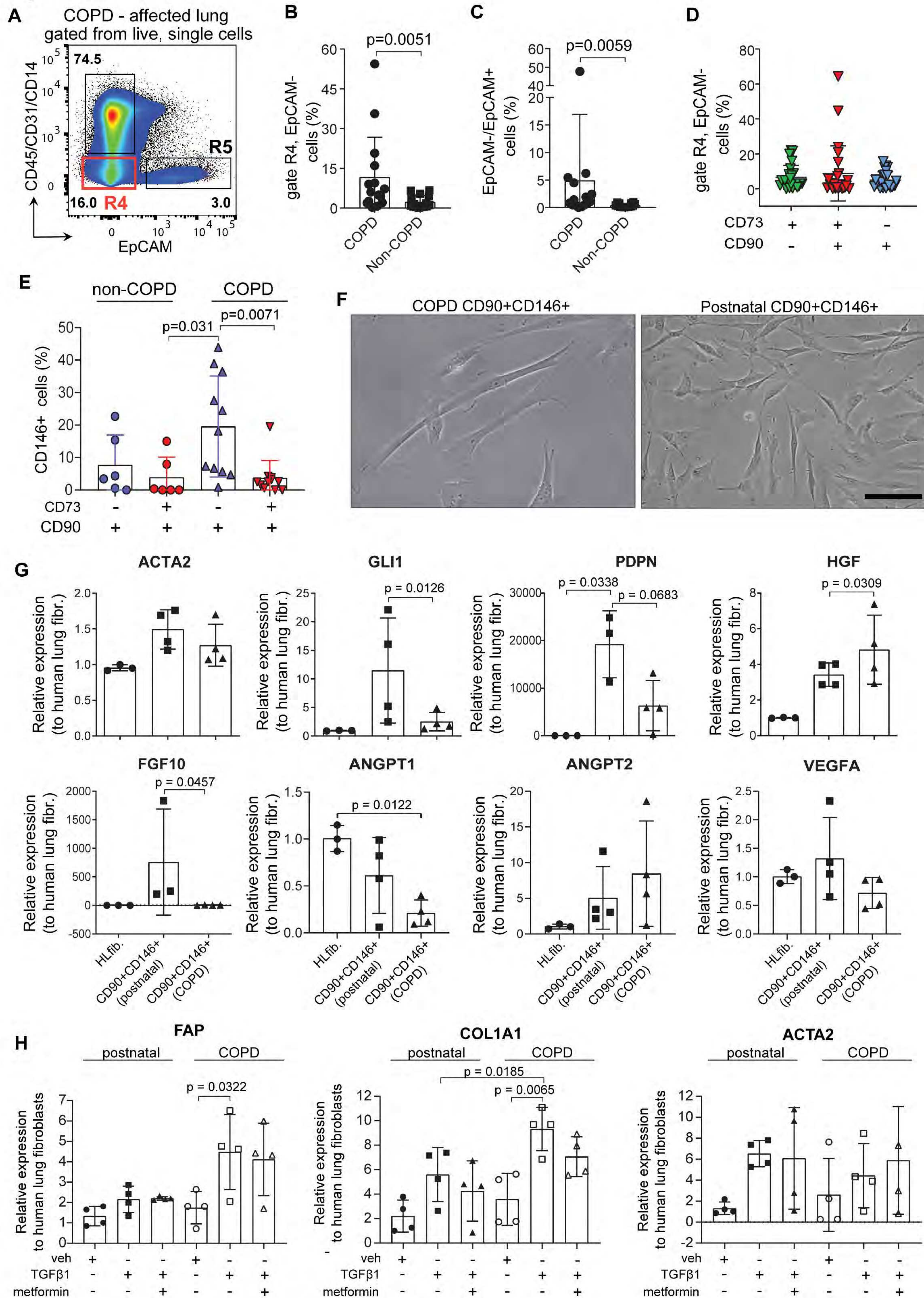
Figure 5

Figure 6

